

Annual Report 2017

Laboratory of Environmental Chemistry

Cover

The dissociation of acids is a central concept in chemistry and plays a pivotal role in environmental chemistry. Because aqueous interfaces feature distinct chemical properties compared to the bulk, interfacial acid–base chemistry is currently only ill-defined. The image illustrates the emerging picture of solvation of acidic trace gases at the air–ice interface as developed based on our recent X-ray photoemission and X-ray absorption experiments at the Swiss Light Source (SLS). We interpret the results from these two complementary methods as physisorbed molecular acid at the outermost ice surface and dissociation occurring upon solvation and diffusion deeper in the interfacial region.

Modifications of the interfacial hydrogen-bonding network seem to be linked to the formation of solvation shells upon entering deeper into the interfacial region. We suggest that the flexibility of water molecules in the quasi-liquid layer is essential to form solvation shells and interpret the confinement of acids to the upper few ice bilayers to be linked with the structure of the hydrogen-bonding network getting more ice-like and rigid with depth. This is in line with strong acids, with their larger energy gain upon dissociation, entering deeper into the air–ice interface than weaker acids.

PAUL SCHERRER INSTITUT



Annual Report 2017

Laboratory of Environmental Chemistry

Editors

M. Schwikowski, M. Ammann

Paul Scherrer Institut

Laboratory of Environmental Chemistry

5232 Villigen PSI

Switzerland

Phone +41 56 310 25 05

www.psi.ch/luc

Reports are available: www.psi.ch/luc/annual-reports



TABLE OF CONTENTS

Editorial.....	1
 Surface Chemistry	
WHEN URBAN AND MARINE AIR MIXES, SO DO THE AEROSOL PARTICLES P. A. Alpert, P. Corral Arroyo, M. Ammann, J. Dou, U. K. Krieger, B. Wang, S. Zhang.....	3
EMISSIONS FROM A JET ENGINE RUN ON ALTERNATIVE FUEL BLENDS P. A. Alpert, P. Corral Arroyo, A. Liati, D. Schreiber, M. Ammann.....	4
MICROFABRICATED ENVIRONMENTAL CELL FOR X-RAY MICROSCOPY P. A. Alpert, B. Watts, J. Raabe, C. Padeste, M. Ammann.....	5
LIMITATIONS OF OZONE DIFFUSION AND REACTION P. A. Alpert, P. Corral Arroyo, J. Dou, U. K. Krieger, S. Steimer, J.-D. Förster, F. Ditas, C. Pöhlker, S. Rossignol, M. Passananti, S. Perrier, C. George, T. Berkemeier, M. Shiraiwa, M. Ammann.....	6
DIFFUSION LIMITATIONS IN IRON CITRATE PHOTOCHEMISTRY P. Corral Arroyo, P. A. Alpert, J. Dou, U. K. Krieger, M. Ammann.....	7
IRON REOXIDATION IN PHOTOCHEMICAL CYCLING J. Dou, P. Corral Arroyo, P. A. Alpert, M. Ammann, U. K. Krieger, T. Peter.....	8
LOW-VOLATILITY PRODUCTS OF IRON CITRATE PHOTOCHEMISTRY Y. Manoharan, P. Corral Arroyo, S. Bjelić, T. Käser, T. Bartels-Rausch, M. Ammann.....	9
IRON AFFECTS PHOTOCHEMICAL OVOC RELEASE FROM SOA P. Corral Arroyo, K. Malecha, M. Ammann, S. Nizkorodov.....	10
FENTON CHEMISTRY AT THE LIQUID-GAS INTERFACE L. Artiglia, S. Chen, H. Yang, K. Roy, P. Corral Arroyo, J. A. van Bokhoven, M. Ammann.....	11
SURFACE PROPERTIES OF HYPOBROMITE AT THE LIQUID-VAPOR INTERFACE S. Chen, I. Gladich, L. Artiglia, F. Orlando, X. Kong, P. Corral Arroyo, K. Roy, H. Yang, J. S. Francisco, M. Vazdar, M. Ammann.....	12
THE EFFECTS OF ORGANICS ON MULTIPHASE CHEMISTRY J. Edebeli, M. Ammann, T. Bartels-Rausch.....	13
A CATIONIC SURFACTANT ACCELERATES BROMIDE OXIDATION S. Chen, J. Edebeli, M. Ammann.....	14
WATER ADSORPTION ON GRAPHITE AT LOW TEMPERATURE H. Yang, L. Artiglia, T. Bartels-Rausch, M. Ammann.....	15
JANUS AT THE INTERFACIAL REGION OF ICE A. Waldner, X. Kong, L. Artiglia, F. Orlando, T. Huthwelker, M. Ammann, T. Bartels-Rausch.....	16
FOSTERING CHEMISTRY IN THE COLD T. Bartels-Rausch, M. M. Frey, J. L. Thomas.....	17
 Analytical Chemistry	
PREFERENTIAL ELUTION OF MAJOR IONS AT THE WEISSFLUHJOCH TEST SITE A. Eichler, J. Trachsel, S. E. Avak, S. Brütsch, J. Edebeli, T. Bartels-Rausch, M. Schneeбели.....	18

REDISTRIBUTION OF MAJOR IONS DURING SNOW METAMORPHISM J. Trachsel, S. E. Avak, J. Edebeli, M. Schneebeli, S. Brütsch, T. Bartels-Rausch, A. Eichler	19
IMPACT OF MELTWATER ON ICE CORE TRACE ELEMENT RECORDS S. E. Avak, M. Schwikowski, A. Eichler	20
EFFECT OF LIGHT-ABSORBING IMPURITIES ON GLACIER ALBEDO A. Dal Farra, A. Marinoni, K. Naegeli, M. Schwikowski	21
NOT GUILTY – THE CASE INDUSTRIAL SOOT VS. ALPINE GLACIER RETREAT M. Sigl, T. M. Jenk, D. Osmont, N. J. Abram, J. Gabrieli, M. Schwikowski	22
BIOMASS BURNING EMISSIONS OBSERVED AT JUNGFRAUJOCH: A CASE STUDY D. Osmont, M. Sigl, S. O. Brügger, R. Modini, M. Schwikowski	23
HOLOCENE BIOMASS BURNING TREND INFERRED FROM AN ANDEAN ICE CORE D. Osmont, M. Sigl, M. Schwikowski	24
EXTRACTION SYSTEM FOR DISSOLVED ORGANIC CARBON IN GLACIER ICE L. Fang, J. Schindler, T. M. Jenk, M. Schwikowski	25
¹⁴ C IN DISSOLVED ORGANIC CARBON (DOC) IN THE FIESCHERHORN ICE CORE L. Fang, T. M. Jenk, M. Schwikowski	26
A METHOD FOR ANALYSING SECONDARY ORGANIC AEROSOLS IN ICE A. L. Vogel, I. El-Haddad, S. Bjelić, K. Arturi, L. Fang, M. Schwikowski	27
CO ₂ IN-SITU PRODUCTION IN GREENLAND ICE T. M. Jenk, T. Blunier	28
VOLCANOES CAST SHADOW ON MONSOON AND CLEOPATRA’S EMPIRE M. Sigl, F. M. Ludlow, J. G. Manning	29
RECONSTRUCTED ACCUMULATION RATES AT THE SUMMIT OF THE QUELCCAYA ICE CAP T. M. Jenk, S. Brütsch, D. Hardy, M. Vuille, M. Schwikowski	30
ICE CORE DRILLING ON TEMPERATE RHONEGLETSCHER M. Schwikowski, T. M. Jenk, D. Stampfli, S. Hellmann, A. Bauder	31
SEARCH FOR A GLACIER IN THE CENTRAL ANDES SUITABLE AS ICE ARCHIVE M. Schwikowski, S. Brütsch, T. M. Jenk, A. Rivera	32
List of Publications	33
Affiliation Index	35

EDITORIAL

For our Laboratory of Environmental Chemistry the year 2017 was a successful one with manifold scientific achievements. Overall we published 20 papers in scientific journals, several of them as outcome of experiments conducted at the Near Ambient Pressure XPS (NAPP) endstation. Among them the study about the ozonide intermediate formed during bromide oxidation at the liquid-gas interface appeared in Nature Communications and the one showing the coexistence of physisorbed and solvated HCl at a warm ice surface in Journal of Physical Chemistry Letters. So, all the long-term investments of the Surface Chemistry Group into developing the liquid-gas and solid-gas interface chambers finally started to pay off. The high potential of NAPP was acknowledged by PSI, resulting in an upgrade into a user facility located at the SLS-NanoXAS beamline from 2018 on, jointly operated by LUC and the Laboratory for Catalysis and Sustainable Chemistry.

The process of integrating our laboratory into the Energy and Environment Research Division (ENE) has continued by strengthening the collaborations with the Laboratory of Atmospheric Chemistry (LAC) and the Laboratory of Bioenergy and Catalysis (LBK) in a project to investigate pre-industrial to industrial changes of secondary organic aerosol tracers in glacier ice cores. This project benefits synergistically from the access to ice cores and expertise in ice core research at LUC, the expertise of secondary organic aerosol at LAC and of ultra high-resolution mass spectrometry at LBK. Such combination of interdisciplinary abilities available at PSI is worldwide unique.

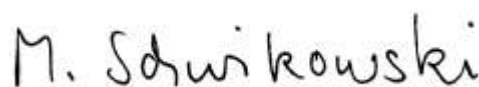
Together with our colleagues from Barnaul, Russia we finally obtained a mercury record showing that emissions from gold/silver mining and from Hg production

have had a strong influence on atmospheric Hg levels in Central Asia from the beginning of the 19th century on. This topic was the initial motivation for collecting the ice core from Belukha glacier in the Siberian Altai in 2001, which proved to be an extremely valuable one with overall 11 publications on very different issues.

The last year also saw the successful PhD defences of Johannes Schindler and Anna Dal Farra at the University of Bern, Astrid Waldner at the ETHZ and of our external student Chaomin Wang at Nanjing University. Our postdoc Peter Alpert received a PSI fellowship within the Marie Skłodowska-Curie Action Horizon 2020 COFUND Program and our postdoc Alexander Vogel left us for a tenure track professor position at the University of Frankfurt. After 16 years working as engineer in the Surface Chemistry group Mario Birrer began his well deserved live as a pensionist last summer.

During the first “Girls on Ice” expedition in Switzerland (<http://www.inspiringgirls.org/switzerland>), nine teenage girls and three instructors spent nine days at Findelen glacier, exploring the glacier and the alpine environment. This was funded by an SNF-Agora project for science communication hosted at PSI.

Our 2-days LUC excursion took us to Rhonegletscher and Oberaarsee, where we were witnessed the dramatic retreat of Alpine glaciers. We concluded the year with a Christmas party at Bossartschüür, in Windisch, organized with great enthusiasm by Peter Alpert and Doris Bühler.



Margit Schwikowski

WHEN URBAN AND MARINE AIR MIXES, SO DO THE AEROSOL PARTICLES

P. A. Alpert (PSI), P. Corral Arroyo (PSI & Univ. Bern), M. Ammann (PSI), J. Dou, U. K. Krieger (ETHZ), B. Wang, S. Zhang (XMU)

The urban environment and continental outflow are host to particles rich in nitrate, sulfate, ammonium, soot and other anthropogenic derived organic matter. We quantify the mixing of particles that reside in marine air impacted by mixed urban and marine sources to better understand their impacts on the environment and climate.

Over oceans, aerosol particles are composed of sea salts and biogenic organic material such as polysaccharides. Almost half of the world's population is coastal and exposed to air impacted by anthropogenic and marine sources. However, the chemical and physical interaction of particles unique to each is rarely evaluated at single particle level in a mixed marine-urban aerosol population. Aerosol particles are often a mixture of e. g. soot, organic and inorganic materials [1]. They can act as liquid and ice forming nuclei affecting cloud formation and precipitation [2]. Quantifying the mixing of these is paramount for predicting aerosol optical properties and thus, contribution to global radiative forcing estimates and climate [3].

We quantify the mixing of particles from three distinctly different air masses using scanning transmission X-ray microscopy with near-edge X-ray absorption fine structure spectroscopy (STXM/NEXAFS). The particles were collected within 200 km offshore of the Guangzhou-Hong Kong urban district in the South China Sea. We classify particles containing one or more components of soot or elemental carbon (EC), organic carbon (OC) and inorganic matter (In). Computer controlled scanning electron microscopy with energy dispersive X-ray analysis (CCSEM/EDX) provided elemental composition. The strength of both techniques is the high statistical significance obtained from hundreds to thousands of individual particles investigated per sample, leading to errors in group abundance of about $\pm 4\%$ at 99% confidence.

Fig. 1 shows mixing of elements C, N, O, S and others in particles as well as those particles clearly identified as sea salt and sea salt/sulfate mixtures. Sea salts and carbonaceous matter contribute a significant fraction by number to the total population from all three types of air masses originating from the Chinese continent or from offshore. Fig. 2 shows that OC is a dominant component, appearing in particles $>90\%$ of the time. Soot particles contribute to about 15-25% of the particles, which indicates the influence of anthropogenic sources. Organic matter associated with sea salt particles may impact liquid and ice clouds. We have found the presence of inorganic particles without any detectable carbon, which was not observed in previous studies [1]. This indicates the presence of fresh emitted coarse mode sea salt particles from ocean waters de-

void of dissolved organic carbon, which are commonly oligotrophic. We note the high number of sea salt particles (Fig. 1) and low number of "In" type particles (Fig. 2) likely reflects the short chemical and physical lifetime of sea salt potentially due to chlorine displacement reactions or cloud activation, respectively.

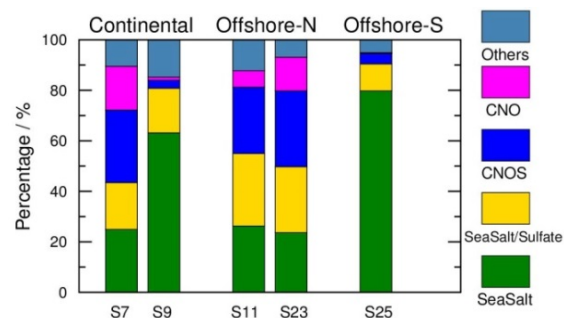


Fig. 1. Number percentage for identified particle types by CCSEM/EDX including sea salt, sea salt mixed with sulfate, organic and sulfur containing organic particles. Sample identification is given below bars.

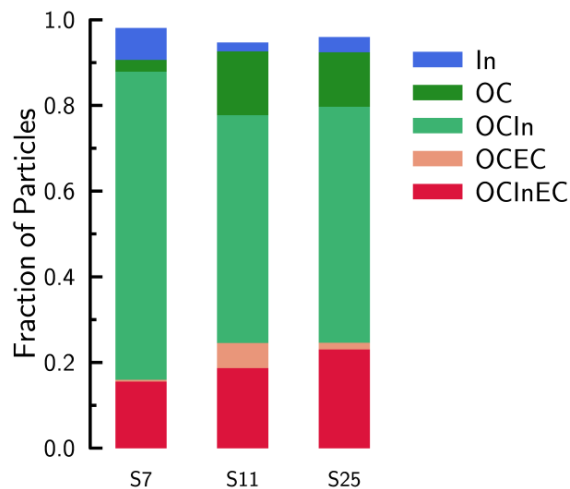


Fig. 2. Number fractions for identified particle types using STXM/NEXAFS.

We acknowledge funding from the Swiss National Science Foundation (Grant 163074), the EU H2020 research and innovation program grant agreement No. 701647 and Chinese Fundamental Research Funds for the Central Universities (Grant 20720160111).

- [1] R. C. Moffet et al., *Atmos. Chem. Phys.*, **16**, 14515-14525 (2016).
- [2] B. Wang et al., *J. Geophys. Res.*, **117**, D00V19, (2012).
- [3] L. Fierce et al., *Nat. Comm.*, **7**, 12361 (2016).

EMISSIONS FROM A JET ENGINE RUN ON ALTERNATIVE FUEL BLENDS

P. A. Alpert (PSI), P. Corral Arroyo (PSI & Univ. Bern), A. Liati, D. Schreiber (EMPA), M. Ammann (PSI)

We present a combined electron microscopic and spectroscopic investigation of particles emitted from a fully operational commercial aircraft engine with an emphasis on soot structure and organic composition.

Half of the world's population enter airports, fly, or come into close proximity of aircraft every year and thus are exposed to aircraft engine emission. The current use of alternative fuels and jet fuel blends such as hydro-processed esters and fatty acids (HEFA) in particular, may result in emission of soot, organic and inorganic particles with characteristic structure or composition. Detrimental health effects are linked to increased exposure to particulate matter. Aircraft particle emission is estimated to cause up to 24,000 premature deaths per year which equates to a loss of \$21 billion using the United States EPA value of statistical life [1]. A dominant factor in the reactivity of soot is morphology, including size and internal structure of primary particles. Primary soot particles are characterised by discontinuous carbon layers in different degrees of structural order, interrupted by amorphous parts probably representing organic compounds [2]. Soot size, degree of structural order, and chemistry, and therefore, reactivity, vary depending on the initial fuel used and engine thrust level [3].

We report on the morphology and composition of soot emitted from an aircraft jet engine situated at SR Technics at Zurich airport as part of the emissions of particulate and gaseous pollutants in aircraft engine exhaust (EMPAIREX) and respiratory health effects of particulate matter generated by aircraft turbine engines (REHEATE) projects. High resolution transmission electron microscopy (HRTEM) and scanning transmission electron microscopy coupled to near edge X-ray absorption fine structure (STXM/NEXAFS) spectroscopy was used to analyse single soot and organic components emitted from the engine run on conventional fuel (Jet-A1) and mixed with HEFA (32%) alternative fuel.

Fig. 1 shows HRTEM images and STXM/NEXAFS spectra of emitted particles. Soot emitted when the engine employed Jet-A1 or blended fuel at near take-off conditions were ordered with graphene-like layers. However, the blended fuel also yielded soot particles with an amorphous outermost rim nanometers thick (yellow line in Fig. 1B). This feature was not observed for the Jet-A1 fuel. Absorption spectra confirm the dominant presence of soot and some oxygenated organic matter in the exhaust. Generally, more hydroxyl and carboxyl functionalities were identified for blended fuel. The presence of organics and the structural alteration of soot particles between the fuel types may

alter soot reactivity. Furthermore, these physico chemical differences may impact toxicity of the soot and other emitted particles.

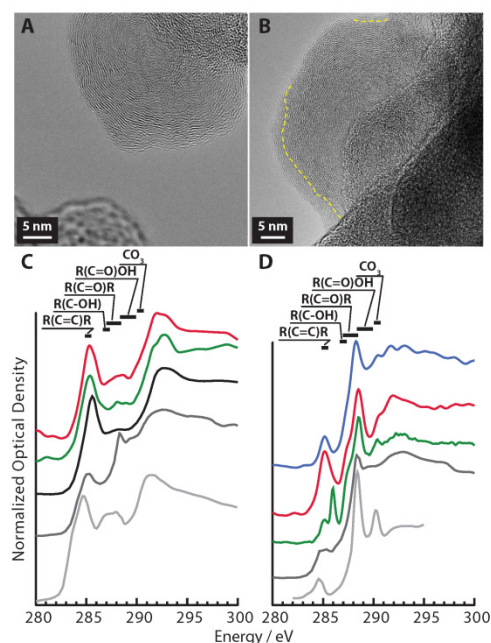


Fig. 1. HRTEM images of soot emitted from the aircraft engine using (A) Jet-A1 fuel and (B) Jet-A1/HEFA blends at take-off conditions. X-ray absorption spectra of soot (C) and soot with organic matter (D) from A1 fuel (blue) and blended fuel (red and green) compared with previous observation of soot or organic matter from Jet-A1 fuel combustion (black) [4], diesel fuel combustion (dark grey) [5] and the ambient atmosphere (light grey) [6]. Peak absorption energy and carbon functionalities are indicated.

We acknowledge funding from the Swiss National Science Foundation (Grant 163074), the EU H2020 research and innovation program (Grant 701647) and the Federal Office of Civil Aviation. SR Technics at Kloten Airport is acknowledged for providing necessary facilities and support.

- [1] S. H. L. Yim et al., *Environ. Res. Lett.*, **10**, 034001 (2015).
- [2] A. Liati et al., *Combust. Flame*, **160**, 671-681 (2013).
- [3] R. L. Vander Wal, V.M. Bryg, M.D. Hays J. *Aerosol Sci.*, **41** (1), 108-117 (2010).
- [4] P. Parent et al., *Carbon*, **101**, 86-100 (2016).
- [5] A. Braun et al., *J. Electron Spectrosc.*, **170**, 42-48 (2009).
- [6] R. C. Moffet et al., *Anal. Chem.*, **82** (19), 7906-7914 (2010).

MICROFABRICATED ENVIRONMENTAL CELL FOR X-RAY MICROSCOPY

P. A. Alpert (PSI), B. Watts, J. Raabe (PSI/LSC), C. Padeste (PSI/LMN), M. Ammann (PSI)

One main goal of this project is to develop an environmental cell using state of the art lithographic fabrication methods with an innovative thermal design concept. Particular focus is placed on observing and localizing ice nucleation on mineral dust particles with and without organic coatings in situ using X-ray microspectroscopic methods.

Ice in clouds is important for precipitation, the hydrological cycle and thus, our earth's climate. Surprisingly, only about 1 in 100,000 particles can form ice in a cloud, which motivates studies to identify those which do freeze on a single particle basis. Previous ice nucleation studies using X-ray microspectroscopy analysis have determined that atmospheric particles which did nucleate ice all were associated with oxygenated organic carbon [1]. These results acquired through off line analysis implied that the organic must have been the primary ice nucleating agent. However, ice nucleation on organic matter in atmospheric particles has never been directly observed. This is likely due to the small spatial constraints of X-ray microscopes, the extreme requirement of T control across a thin X-ray transparent film (~ 100 nm) and finally the low water vapor pressure at about 200-270 K where ice forms.

Scanning transmission X-ray microscopy with near edge X-ray absorption fine structure spectroscopy (STXM/NEXAFS) is a powerful tool to quantify chemical morphology of aerosol particles, such as mineral dust particles with organic coatings, and to observe the locations where ice forms with a resolution of tens of nanometers [2]. Careful control of T and RH is necessary in ice nucleation experiments, motivating the fabrication of a new environmental micro-reactor. Heat transfer simulations [3] (Fig. 1A) are used to ensure that for a given stable silicon frame temperature, T_{frame} , the 100 nm thick sample area with a thermally conductive pad and patterned temperature sensor could maintain a near uniform temperature gradient, ΔT . In addition, the coldest spot on the sample area is located exactly at the center, a requirement to ensure that ice forms there and not at e.g. fabricated corners or edges within the cell. The heat transport occurs from the frame along the thermally conductive Al layer (Fig. 1B) toward the center and second, loss from the continuous flow of humidified gas inside the cell warmer than the sample area.

The cell is closed using a second silicon frame/silicon nitride membrane and a micrometer scale layer of polydimethylsiloxane (PDMS) acting as a seal as illustrated in Fig. 1B. The PDMS will form an air channel ensuring humidified air only at the sample area. We expect that T_{frame} and sample cooling used should define ΔT beneath the PDMS and sample area. In our

simulation $T_{\text{frame}}=200$ K and a cooling power equivalent to $P=0.1 \mu\text{W cm}^{-2}$ resulting in $\Delta T < 0.1$ K over the sample area ($0.2 \times 0.2 \mu\text{m}$). Additional developments for a 4 point contact sensor and other technical design aspects are ongoing. An isolated sample area with small ΔT makes observations of ice nucleation in an X-ray microscope possible for the first time.

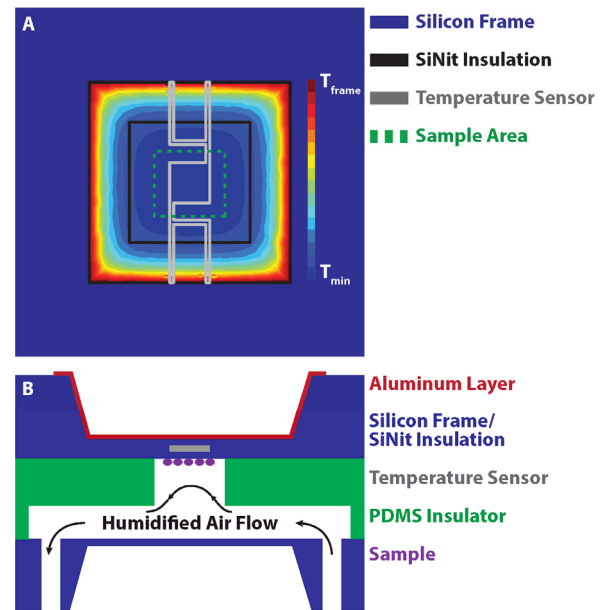


Fig. 1. Heat transfer simulation over a 1x1mm area and conceptual cell design. A) The color scale shows exemplary T below T_{frame} . Black solid and grey solid lines outline silicon nitride electrical insulation and the Pt temperature sensor, respectively. The dashed green line indicates the sample area. B) Side view indicating the silicon frame, the PDMS seal, sample particles and nanometer scale layers of silicon nitride, platinum (temperature sensor) and aluminum. Dimensions are not to scale.

We acknowledge funding from the Swiss National Science Foundation (Grant 163074) and the European Union's Horizon 2020 research and innovation program grant agreement No. 701647.

- [1] D. A. Knopf et al., *Earth. Space. Chem.*, 10.1021/acsearthspacechem.7b00120 (2018).
- [2] J. Raabe et al., *Rev. Sci. Instrum.*, **79**, 113704 (2008).
- [3] C. Baldasseroni et al., *Rev. Sci. Instrum.*, **82**, 093904 (2011).

LIMITATIONS OF OZONE DIFFUSION AND REACTION

P. A. Alpert (PSI), P. Corral Arroyo (PSI & Univ. Bern), J. Dou, U. K. Krieger (ETHZ), S. Steimer (ETHZ & PSI), J.-D. Förster, F. Ditas, C. Pöhlker (MPIC), S. Rossignol, M. Passananti, S. Perrier, C. George (IRCELYON), T. Berkemeier (GIT), M. Shiraiwa (UCI), M. Ammann (PSI)

Aerosol organic matter may be highly viscous, limiting chemical reactions occurring within particles. We show that when ozone and water is taken up by organic particles, reaction and diffusion of ozone may be limited to the surface region tending toward a gradient or non-uniform concentration.

Atmospheric aerosol particles are composed of a variety of inorganic and organic components. Organic matter in particles stems from a variety of natural and anthropogenic sources and is found in significant quantities in almost every single aerosol particle [1]. The fate of particles residing in the atmosphere is largely dependent on physical processes such as rain-out or gravitational settling. During their atmospheric lifetime the particles can undergo chemical changes as well, which may change the particle hydrophilicity or surface composition and affect their ability to form liquid or ice clouds. A chemical change may also alter the toxicity of particles, which can be a danger to humans exposed to them [1]. We present a model investigation of the diffusion of O_3 , an oxidizing atmospheric trace gas, into xanthan gum particles, a model organic/biogenic marine derived particle. Using a kinetic multi-layer model which resolves gas transport to the particle and reaction within [2], we track O_3 reaction with Fe(II) homogeneously mixed in the Xanthan gum matrix. Fe(II) acts as a tracer of where O_3 has been and reacted. Parameters such as Henry's law coefficient, H , and O_3 and Fe diffusion coefficients, D_{O_3} and D_{Fe} , respectively, through the xanthan gum matrix are key for predicting internal reaction profiles.

Fig. 1 shows our data taken using scanning transmission X-ray microscopy with near edge X-ray absorption fine structure (STXM/NEXAFS) spectroscopy in a custom aerosol environmental cell containing O_3 at 150 ppb, relative humidity (RH) at 80%, O_2 at 40 mbar and He at 110 mbar. Xanthan gum and Fe(II) particles ($FeCl_2$) 0.2-2 μm in diameter exposed to O_3 resulted in a decrease of the Fe(II) fraction from about 0.8 to 0.3 over the course of 3 hours. This trend was captured using our model assuming $H=1.4\times 10^{-4}$ mol cm^{-3} atm $^{-1}$, $D_{O_3}=9\times 10^{-7}$ cm 2 s $^{-1}$ and $D_{Fe}=7\times 10^{-15}$ cm 2 s $^{-1}$. These values are typical for a semi-solid material which is close in viscosity to tar. Similar values were found for O_3 diffusion through shikimic acid [3]. Fig. 1 also shows the calculated radial profiles of Fe(II) fraction and O_3 concentration in a 1 μm diameter particle. Note that a strong gradient is predicted to develop over time where the core of the simulated particle is left unreacted while the particle surface is entirely oxidized. This represents a possible situation in which reaction and diffusion of both reactants are limiting, inducing a gradient of both. This is seen by the normalized ozone concentration, $[O_3]/[O_3]_{max}$, where unity indicates

Henry's Law equilibrium. Ozone is only present at the particle surface which implies the gradient develops largely due to Fe diffusion. Our results demonstrate reactions with organic particles can be limited, thus increasing their lifetime beyond what can be expected when assuming homogeneously mixed particles. This should impact predictions of aerosol chemical aging during atmospheric transport.

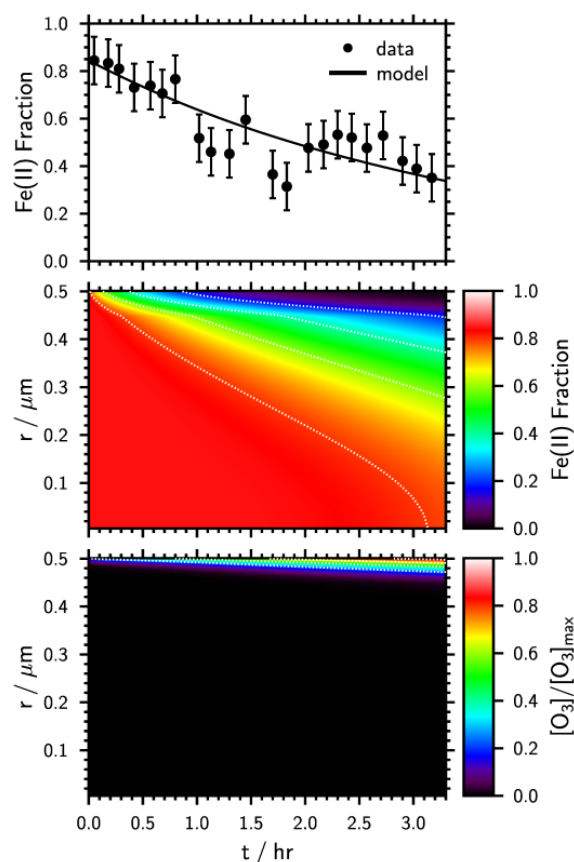


Fig. 1. (Top) Depletion of Fe(II) as a function of ozone exposure time, t . (Middle) Calculated radial profiles of Fe(II) fraction over t . (Bottom) Normalized radial profiles of ozone concentration.

We acknowledge funding from the Swiss National Science Foundation (Grant 163074) and the European Union's Horizon 2020 research and innovation program grant agreement No. 701647.

- [1] A. Laskin et al., *Annu. Rev. Anal. Chem.*, **9**, 117-143 (2016).
- [2] M. Shiraiwa et al., *Atmos. Chem. Phys.*, **10**, 3673-3691 (2010).
- [3] S. S. Steimer et al., *Atmos. Chem. Phys.*, **14**, 10761-10772 (2014).

DIFFUSION LIMITATIONS IN IRON CITRATE PHOTOCHEMISTRY

P. Corral Arroyo (PSI & Univ. Bern), P. A. Alpert (PSI), J. Dou, U. K. Krieger (ETHZ), M. Ammann (PSI)

Fe(III) plays an important role in aerosol phase radical production [1] and degradation of carboxylic acids [2]. This work studies the feedbacks between UV-VIS photochemistry initiated by Fe(III) citrate and aerosol particle microphysics.

Iron (Fe(III)) carboxylate complexes absorb light below about 500 nm, which is followed by ligand to metal charge transfer (LMCT) resulting in Fe(II) and oxidation of the carboxylate ligands, an important sink of organic acids in the troposphere [1]. The volatile organic products as well as CO₂ are released, contributing to particle mass loss. Fe(II) can be re-oxidized to Fe(III) closing the catalytic cycle (Fig. 1).

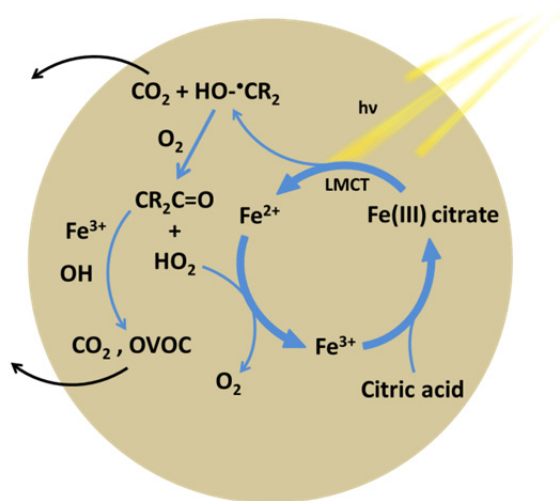


Fig. 1. Photocatalytic mechanism of citric acid oxidation induced by Fe(III) citrate complexes.

Our multi-technique approach involves Coated Wall Flow Tube (CWFT) and Scanning Transmission X-Ray Microspectroscopy (STXM) experiments as well as a single particle levitation technique reported on page 8. The inner surface of the CWFT is coated with a film composed of a mixture of iron citrate (FeCit) and citric acid (CA), and we measure the HO₂ release while exposing the film to UV light at different conditions. HO₂ is measured by scavenging in an excess of nitrogen monoxide (NO) followed by detecting NO₂. For STXM we expose single FeCit/CA (1:1) particles to UV (370 nm, 3Wm⁻²) for 15 minutes at 40% RH (110 mbar of O₂) in He and map the Fe(III) fraction (Fe(III)/(Fe(II)+Fe(III))) over the particles through spectral changes at the Fe L-edge [3].

Fig. 2 shows the HO₂ release as a function of the film thickness, at constant FeCit/CA ratio, UV irradiance and RH (40%). Radical release saturates above 1 μm, indicating either depletion of oxygen over this depth or radical recombination on the way towards the surface. From the STXM experiments, we observed a gradient in the Fe(III) fraction decreasing from the surface of

the particle towards the bulk (Fig. 3). This indicates that the O₂ concentration is high enough only near the surface to reoxidize Fe(II) to Fe(III) and depleted towards the bulk. The reacto-diffusive length observed by STXM (~400 nm) differs from the one inferred by the CWFT experiments (~900 nm) due to differences in the initial Fe(III) content and oxygen concentration as well as the photolysis rate (j_{FeCit}), which will be considered in further analysis.

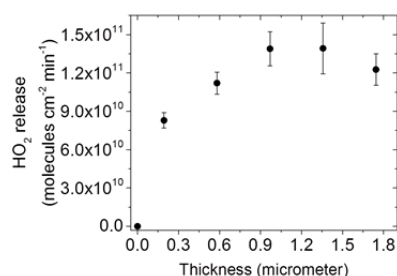


Fig. 2. HO₂ release from mixtures of FeCit/CA ($\chi_{\text{FeCit}}=0.07$) at 40% RH versus thickness of the film in the coated wall flow tube.

We conclude that diffusion and reaction are coupled also in photochemical aging processes. In addition, if condensed phase radical production is substantial, the concentration of O₂ scavengers may get high enough to induce anoxic bulk chemistry in the interior of viscous atmospheric aerosol particles.

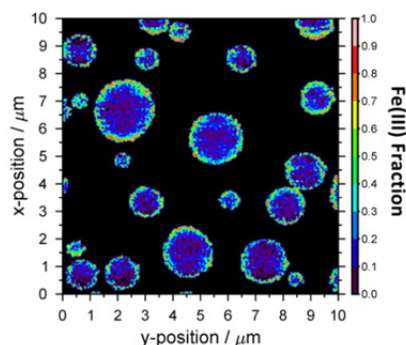


Fig. 3. Map of FeCit/CA (1:1) aerosol particles after UV irradiation at 40% RH. The color scale indicates Fe(III) fraction (Fe(III)/(Fe(II)+Fe(III))).

We acknowledge funding from the Swiss National Science Foundation (Grant 163074).

- [1] C. Weller et al., *Environ. Sci. Technol.*, **48** (10), 5652-5659 (2014).
- [2] H. Hermann et al., *J. Atmos. Chem.*, **36** (3), 231-284 (2000).
- [3] R. Moffet et al., *J. Geophys. Res.*, **177** (D7), (2012).

IRON REOXIDATION IN PHOTOCHEMICAL CYCLING

J. Dou (ETHZ), P. Corral Arroyo (PSI & Univ. Bern), P. A. Alpert, M. Ammann (PSI), U. K. Krieger, T. Peter (ETHZ)

Fe(III)-citrate (Fe(III)Cit) photochemistry plays an important role in aerosol aging, especially in the lower troposphere, having a significant impact on gas-particle partitioning of organic compounds. We simulated Fe(III)Cit photochemistry in laboratory experiments and investigated Fe(III) recovery efficiency related to varying relative humidity.

Fe(III)Cit complex acts as a photocatalyst for oxidation processes. It can easily get excited by light below 500 nm, inducing the reduction of Fe(III) and oxidation of carboxylate ligands [1]. When O₂ is present, ensuing radical chemistry will likely lead to more decarboxylation, peroxides and oxygenated volatile organic compounds (OVOC) production. The radicals (e. g. OH•, HO₂•, RO₂•) in turn allow re-oxidation of Fe(II) to Fe(III), closing this photocatalytic cycle.

First we used a single, levitated aerosol particle in an electrodynamic balance (EDB). The mass and size changes of an aqueous Fe(III)Cit/citric acid (CA) particle were observed over time. We exposed the particle to blue laser irradiation (473 nm, 4×10^4 W m⁻²) in N₂ for 500 s until all Fe(III) was reduced, then switched N₂ to O₂ waiting for different recovery time periods, then switched back to N₂ again, and repeating the procedure. Generally, a mass loss during Fe(III)Cit photochemistry occurred due to evaporation of volatile (e.g. CO₂) and semi-volatile (e.g. ketones) products.

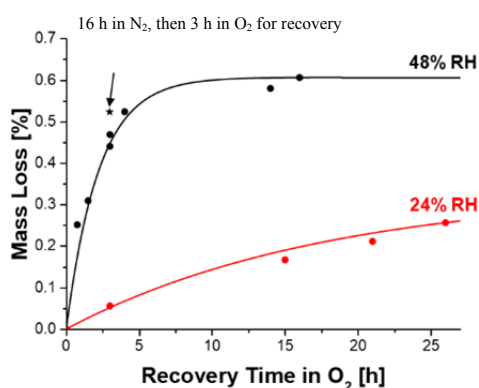


Fig. 1. Mass loss of Fe(III)Cit/CA (0.05:1) particle due to Fe(III) photochemistry after recovered in O₂ for different time periods at 48% RH (black dots) and 24% RH (red dots).

As Fig. 1 shows, with relative humidity (RH) constant, particle mass loss during each irradiation depended on the recovery time span in O₂ before that irradiation: with increased recovery time, mass loss increased as there was more Fe(III) available. At RH=48%, 10 h exposure to O₂ was sufficient for Fe(III) to be reoxidized, while at RH=24%, the recovery after 25 h was not yet complete. This can be attributed to molecular diffusion limitations at lower RH.

Recovery of Fe(III) was observed in scanning transmission X-ray microscopy (STXM). Fe oxidation state inside Fe(III)Cit/CA particles exposed to UV light in O₂ was measured by STXM. Fig. 2 indicates a fast recovery of Fe(III) after UV exposure in O₂. The recovery is slower in the absence of O₂ during UV and introducing O₂ ($\sim 3 \times 10^{-3}$ min⁻¹) only after 45 min or 9 h. This implies that oxidation through radical chemistry may significantly impact Fe cycling, and that the life time of these radicals may be <9 h. However, it should be noted that in Fig.1, waiting in N₂ for 16 hours after irradiation (black star), the recovery was still comparable to O₂ exposure right after the irradiation (black circles), which suggests that direct oxidation by O₂ may also be significant in this system. This apparent contradiction between EDB and STXM results may be due to the different Fe(III)Cit/CA ratios (0.05 in EDB vs. 1 in STXM), different sizes of the particles (~ 10 μm in EDB vs. ~ 1 μm in STXM), and/or other different conditions like different O₂ concentrations in the system.

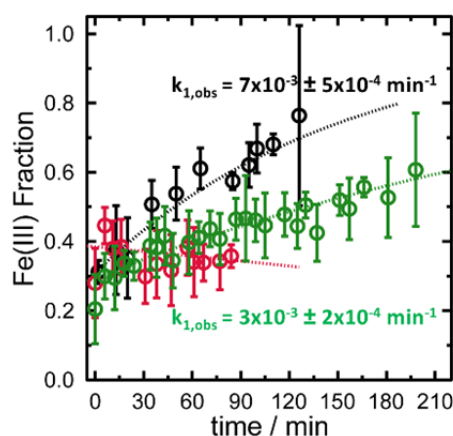


Fig. 2. Fe(III) fraction in Fe(III)Cit/CA (1:1) particles versus recovery time in O₂, after exposure to UV irradiation (370 nm, 3 W m⁻²) for 15 min. Black circles: particles exposed to UV light at 60% RH with O₂ present, then investigated right after light off with same RH with O₂ present; Green and red circles: particles exposed to UV light at 40% RH in N₂, followed by 45 min (green) waiting in the dark still in N₂, then exposed to increased RH (60%) and O₂, during the measurements shown.

We acknowledge funding from the Swiss National Science Foundation (Grant 163074).

[1] C. Weller et al., *Environ. Sci. Technol.*, **48**, 5652-5659 (2014).

LOW-VOLATILITY PRODUCTS OF IRON CITRATE PHOTOCHEMISTRY

Y. Manoharan, P. Corral Arroyo (PSI & Univ. Bern), S. Bjelić, T. Käser (PSI/LBK), T. Bartels-Rausch, M. Ammann (PSI)

Iron (Fe) photochemistry is an important process in the atmosphere since it represents a major sink of carboxylic groups in aerosol particles [1]. This work investigates the products of the degradation of citric acid (CA) by photolysis of the corresponding complexes with Fe(III) by HPLC-MS.

Iron complexes are important species in indirect photochemical oxidation of organic compounds in atmospheric particles. Fe(III) carboxylate (citrate among them) complexes absorb light below about 500 nm, which is followed by ligand to metal charge transfer (LMCT) resulting in the reduction of iron to Fe(II) and oxidation of the carboxylate ligands as represented in Fig. 1, which represents a major contribution to the degradation of carboxylic acids in the atmosphere [1] and to aerosol aging via secondary radical cycles [2].

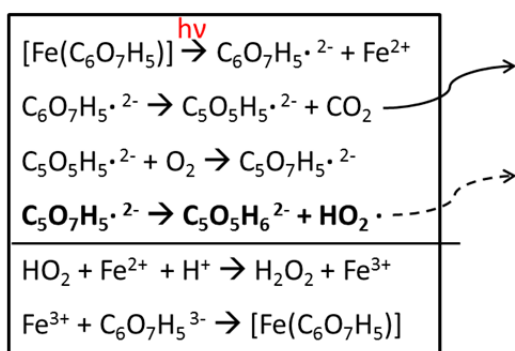


Fig. 1. Mechanism of photo-degradation of iron-citrate: FeCit absorbs UV-VIS leading to LMCT and thus Fe(II) and the corresponding radical after decarboxylation, which in turn produces a HO₂ radical by reacting with oxygen. Fe(II) can be re-oxidized to Fe(III) by HO₂ or H₂O₂.

We deposited mixtures of Fe(III) citrate (FeCit) and CA (1:10) on the inner surface of a flow tube, which we exposed to UV light for varying times (from minutes to hours) under humidified (40% RH) synthetic air (O₂ (100 ml/min) and N₂ (400 ml/min)), with the set-up shown in Fig. 2. The tube is surrounded by seven UV lamps and the temperature within the tube was controlled by a thermostat set to 25°C. After irradiation, we extracted the film with a mixture of water and acetonitrile (1:1). Vanillin was added to the extract in order to have an internal standard at fixed concentration.

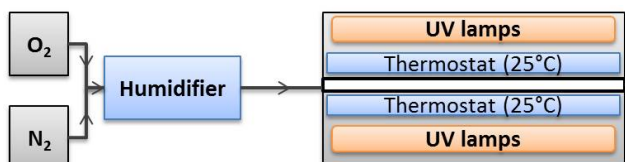


Fig. 2. Irradiated coated wall flow tube set-up.

The analysis of the extracted solution was performed with a HPLC-QP-MS. We optimized the composition of the column using a ciano column.

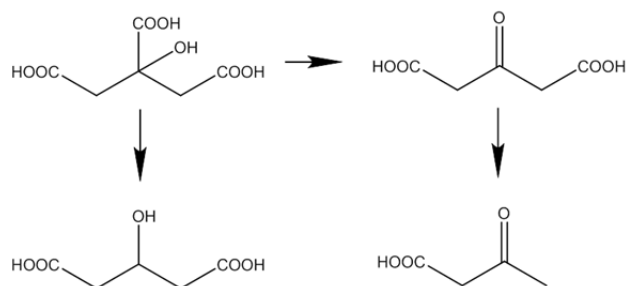


Fig. 3. Molecules found in the HPLC extracts integrated in a degradation mechanism of citric acid.

We observed that the citric acid concentration decreased during irradiation and that the signal of several masses increased indicating the generation of products of the degradation of CA. Some of these compounds are expected to be produced by the photo degradation of iron citrate (Fig. 1 and 3) and also appear as products of OH initiated citric acid degradation [3]. Compounds coming from condensation reactions were observed, which indicate the production of compounds containing double bonds, likely produced by intramolecular radical self-reaction, or compounds coming from intramolecular esterification. We also found evidence for compounds with higher masses, indicating the presence of poly-iron complexes, which may have an impact on the viscosity and thus diffusivity in the system, and possible radical recombination.

Further experiments must be performed to determine products formed in different oxidation generations and assess the composition after long irradiation times.

We acknowledge funding from the Swiss National Science Foundation (Grant 163074).

- [1] C. Weller et al., *Environ. Sci. Technol.*, **48**, 5652-5659 (2014).
- [2] D. Jacob: *Introduction to Atmospheric Chemistry*, Princeton University Press, Princeton, N.J. (1999).
- [3] M. J. Liu et al., *J. Phys. Chem. A*, **121**, 5856-5870 (2017).

IRON AFFECTS PHOTOCHEMICAL OVOC RELEASE FROM SOA

P. Corral Arroyo (PSI & Univ. Bern), K. Malecha (UCI), M. Ammann (PSI), S. Nizkorodov (UCI)

Fe(III) catalyzes the photo degradation of organic compounds in atmospheric aerosol particles. We quantify the influence of Fe(III) on the photoinduced release of oxygenated volatile organic compounds (OVOCs) from Secondary Organic Aerosol (SOA) material produced by limonene ozonolysis.

The photolysis of organic chromophores in SOA leads to singlet oxygen or HO_x radical chemistry, in turn leading to degradation of non-volatile compounds and release of volatile OVOCs such as formic acid, acetaldehyde, acetone and acetic acid [1]. The most important chemical processes of Fe(III) in atmospheric particles (Fig.1) are the photo degradation of Fe(III) carboxylate complexes [2] and Fenton chemistry [3].

In this work we produced SOA from limonene and ozone in a flow tube reactor and collected it on a substrate. The resulting material was exposed under dry conditions and 55% RH at 25°C to several mW of near-UV radiation ($\lambda \sim 310\text{nm}$) from a light-emitting diode. Fe(III) was added to the material by dropping different volumes of a solution of FeCl₃ (10^{-3} M, pH=5.15). The control experiment was based on the addition of similar volumes of ultrapure water. We followed the release of formic acid, acetaldehyde, acetone and acetic acid by means of a Proton Transfer Reaction Mass Spectrometer (PTR-MS). The total mass loss was measured by a Quartz Crystal Microbalance (QCM) and compared with the estimated mass loss by PTR-MS measurements in absence of Fe(III) and at 10% molar ratio of Fe(III) assuming an average molar mass of 100 g mol^{-1} for the organics present in the SOA.

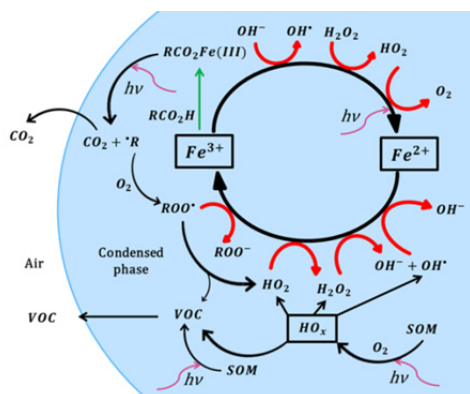


Fig. 1. Chemical cycling of Fe³⁺/Fe²⁺ involving reactions with HO_x and photochemistry of iron carboxylate complexes.

After switching on light, signals for each species increased and reached a steady state after 5-20 min. Under dry conditions we observed that the steady state release of OVOC species generally decreased with

increasing Fe(III) content, except for acetic acid, which exhibited a slight increase at 2% of Fe(III). At 55% RH this trend was more pronounced with a higher enhancement and for every compound (Fig. 2).

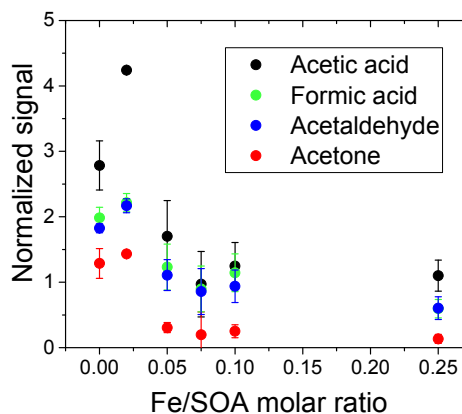


Fig. 2. Steady state signal of the 4 OVOCs released at 55% RH and 25°C upon illumination normalized to the dry mass of collected SOA material with different Fe:SOA molar ratios (%).

Measurements by the QCM indicate that the mass loss is reduced by 80% when Fe(III) is present in a mole ratio of 10% in comparison with mass loss in absence of iron. Converting the OVOC measured by PTR-MS to OVOC mass release indicates that OVOC release represents 21.4% of the total mass loss in absence Fe(III), but only 5.0% in presence of Fe(III).

The presence of iron contributes to OVOC production by adding a new degradation pathway through the photolysis of the iron carboxylate complexes, which increases also the CO₂ production within the particles. At high concentrations of iron, it is not fully complexed, so that the free iron cycles between Fe²⁺ and Fe³⁺, thereby shutting down the radical chemistry started by chromophores, and thus deactivating the production of OVOC. The remaining OVOC is mainly attributed to iron carboxylate photolysis.

We acknowledge funding from the Swiss National Science Foundation (Grant 163074).

- [1] C. Malecha et al., *Environ. Sci. Technol.*, **50** (18), 9990-9997 (2016).
- [2] C. Weller et al., *Environ. Sci. Technol.*, **48** (10), 5652-5659 (2014).
- [3] H. Hermann et al., *J. Atmos. Chem.*, **36** (3), 231-284 (2000).

FENTON CHEMISTRY AT THE LIQUID-GAS INTERFACE

L. Artiglia (PSI), S. Chen, H. Yang (PSI & ETHZ), K. Roy (ETHZ), P. Corral-Arroyo (PSI & Univ. Bern), J. A. van Bokhoven (PSI/LSK & ETHZ), M. Ammann (PSI)

This work aims to develop a new approach to characterize Fenton's reagents at the liquid-gas interface by means of ambient pressure x-ray photoelectron spectroscopy.

The Fenton's reaction produces either highly-valent iron species (ferryl, FeO^{2+}) or Fe^{3+} and $\cdot\text{OH}$ radicals. The study of Fenton chemistry is of wide interest, due to the presence of Fe^{2+} and peroxides both in vivo and in the environment. In spite of its importance, the mechanism at the basis of Fenton reactions has not been fully understood yet. Depending on the reaction conditions, the Fe^{2+} ions undergo either a one-electron transfer (producing Fe^{3+} and $\cdot\text{OH}$ radicals) [1] or a two-electron oxidation (yielding high-valent FeO^{2+} species) [2]. The preferential formation of either ferryls or Fe^{3+} reflects on the course of oxidative chemistry. Recent experiments claim that, due to the partial hydration sphere of Fe^{2+} at the water-air interface, ferryls are preferentially formed while hydrogen peroxide is dosed from the gas phase [3]. A surface sensitive non-invasive technique is required to confirm this conclusion. This project aims to use surface sensitive techniques (x-ray photoelectron spectroscopy XPS and near edge x-ray absorption fine structure spectroscopy NEXAFS) to investigate Fenton's reagents solutions. The liquid microjet setup available at the near ambient pressure photoemission endstation (NAPP) allows to inject liquid solutions either in vacuum or while dosing a gas stream around. The microjet produces a liquid filament running at high speed, thus limiting the beam damage effects caused by the high photon flux available at the SIM beamline (Swiss Light Source).

We acquired the photoemission and absorption spectra of 5 samples: 2 reference solutions (0.3 mol/L Fe^{2+} and Fe^{3+}), 0.3 mol/L Fe^{2+} + gaseous hydrogen peroxide, and 2 Fenton's reagents (mixtures of Fe^{2+} and hydrogen peroxide) having different $[\text{Fe}^{2+}]/[\text{H}_2\text{O}_2]$ ratios of 3:1 and 1:2, respectively. The photoemission spectra of the Fe 2p levels are shown in Fig. 1 on the left. The spectra of the two reference solutions show that there is a big chemical shift (about 5.6 eV) between the two centroids. No evident change is observed between the spectra of the Fe^{2+} solution acquired before and while dosing hydrogen peroxide from the gas phase, probably due to the small H_2O_2 pressure achieved during this experiment (about 1.5×10^{-4} mbar). A positive shift of the binding energy is detected passing from a 3:1 to a 1:2 $[\text{Fe}^{2+}]/[\text{H}_2\text{O}_2]$ ratio of the Fenton's reagent. However, even in the presence of an excess of hydrogen peroxide, the spectrum does not match that of Fe^{3+} . Within the probed depth of photoemission ($3\lambda = \text{ca. } 6 \text{ nm}$), the main product of the reaction is not Fe^{3+} . Competitive reactions are probably reducing the Fe^{3+} . The spectra of the Fenton's reagents could be either

those of a complex mixture of products or may suggest that new species (ferryls) form, which stay preferentially at the surface. The absorption spectra of the Fe $L_{2,3}$ edge are shown in Fig. 1 right. In agreement with XPS, the spectrum acquired while dosing gaseous hydrogen peroxide is similar to that of Fe^{2+} . The NEXAFS of the 3:1 Fenton's reagent displays relevant changes as compared to that of the Fe^{2+} solution. Its shape suggests the concomitant presence of Fe^{2+} and Fe^{3+} , in contrast with photoemission. Such a difference could be explained by the different probed depth between XPS and NEXAFS (the latter being more bulk sensitive due to larger kinetic energy of Auger electrons used for the NEXAFS spectra (585 eV) than that of XPS (ca. 280 eV). Within the information depth of XPS iron has a ferrous-like behavior, whereas more in the bulk it is ferric-like (NEXAFS). Interestingly, highly valent iron-oxygen species have a ferrous-like behavior [4]. The absorption spectrum of the 1:2 Fenton's reagent is almost identical to that of Fe^{3+} . Also this is not in full agreement with the XPS results.

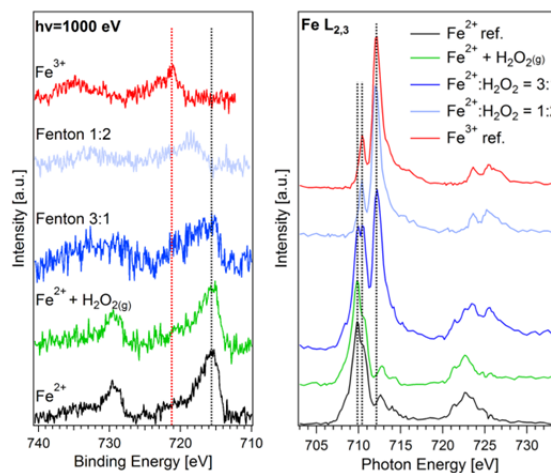


Fig. 1. (left) Fe 2p photoemission spectra of the reference solutions (Fe^{2+} and Fe^{3+}), of a Fe^{2+} solution exposed to gaseous hydrogen peroxide and of Fenton's reagents; (right) x-ray absorption spectra of the same solutions, for which XPS spectra are shown on the left.

The results obtained warrant further investigations to include kinetic energy dependent XP spectra of the Fe 2p, the investigation of other $[\text{Fe}^{2+}]/[\text{H}_2\text{O}_2]$ ratios and of the reaction between Fe^{2+} aqueous solution and higher pressures of gaseous H_2O_2 .

- [1] F. Haber, J. Weiss, Proc. Roy. Soc. A. **134**, 332 (1934).
- [2] W. C. Bray, M. H. Gorin, J. Amer. Chem. Soc. **54**, 2124 (1932).
- [3] S. Enami et al., PNAS **111**, 623 (2011).

SURFACE PROPERTIES OF HYPOBROMITE AT THE LIQUID-VAPOR INTERFACE

S. Chen (PSI & ETHZ), I. Gladich (HBKU), L. Artiglia, F. Orlando (PSI), X. Kong (PSI & Univ. Gothenburg), P. Corral Arroyo (PSI & Univ. Bern), K. Roy (ETHZ), H. Yang (PSI & ETHZ), J. S. Francisco (UNL), M. Vazdar (RBI), M. Ammann (PSI)

The multiphase oxidation of bromide to hypobromite by ozone in sea water, sea spray or marine aerosol occurs preferentially at the interface. Here, we assess the surface propensity of hypobromite at the aqueous solution-air interface by liquid jet XPS.

Oxidation of bromide (Br^-) to hypobromite (OBr^-) is one of the important reactions to produce molecular halogen compounds that later drive O_3 depleting chemistry in the troposphere [1]. The intermediate $[\text{Br}\cdot\text{OO}\cdot]$ of this reaction has a strong preference for the liquid-vapor interface [2]. Here, we use liquid jet X-ray photoelectron spectroscopy (XPS) at the Swiss Light Source (SLS) [3] to assess the surface propensity of OBr^- .

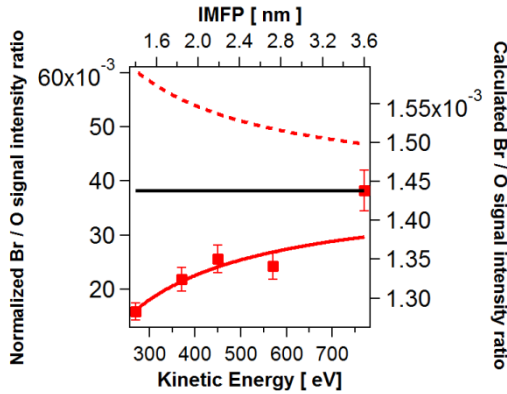


Fig. 1. Br 3d photon emission (PE) signal intensity of OBr^- (red squares) in mixed 0.08 M NaOBr and NaBr solutions normalized by the condensed phase O 1s PE signal of H_2O , the photon flux, and the cross section as a function of the kinetic energy (error bar: 10%, left y-axis); calculated Br / O signal intensity ratio as a function of the inelastic mean free path (IMFP, λ , right y-axis, top x-axis) (dashed and solid red line for a surface excess of + and $-7.2 \times 10^{12} \text{ cm}^{-2}$, respectively, and black line for zero surface excess).

We acquired Br 3d core level spectra of 0.08 M solutions composed of equal amounts of NaOBr and NaBr. The Br 3d region was fit by two spin-orbit split doublets, with the peak assigned to OBr^- separated by 2.2 eV from that of Br^- . The probe depth was varied by varying the photoelectron kinetic energy, E_k , and thus inelastic mean free path (IMFP, λ) via variation of the probing photon energy. The Br 3d to O 1s signal intensity ratio increases with E_k (Fig. 1). The photoemission (PE) intensity, I , of a solute can be split into contributions from surface and bulk. When attenuation of photoelectrons originating from the surface molecules is neglected, the surface contribution is proportional to the surface excess (Γ_X). The bulk contribution is proportional to $(n_{b,X} \times \lambda)$, where $n_{b,X}$ is the bulk number density of the solute. Thus the ratio of $I_{\text{Br}3d}$ and $I_{\text{O}1s}$, the PE signal intensities for hypobromite and H_2O of

liquid water, respectively, each normalized to photon flux and ionization cross section is then:

$$\frac{I_{\text{Br}3d}}{I_{\text{O}1s}} = \frac{(\Gamma_{\text{BrO}^-} + n_{b,\text{BrO}^-} \times \lambda)}{n_{b,\text{H}_2\text{O}} \times \lambda} \quad (1)$$

with $n_{b,\text{H}_2\text{O}}$ denoting the bulk number density of H_2O molecules. In Fig. 1, this ratio is shown for three hypothetical cases, featuring positive, zero and negative surface excess. Thus, OBr^- appears to exhibit net depletion from the surface.

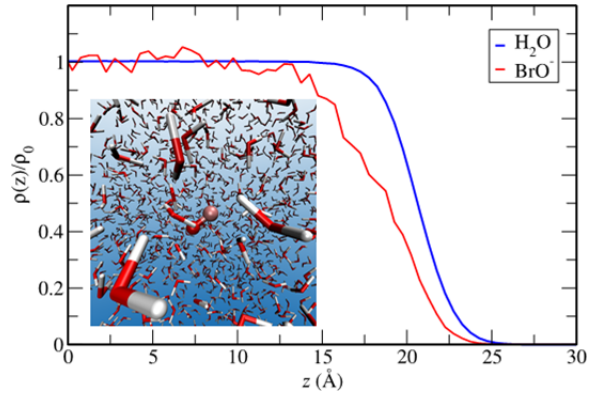


Fig. 2. The density profiles for BrO^- ions and H_2O in water and snapshot of the classical MD simulation for BrO^- .

Molecular dynamics (MD) simulations were performed to investigate the bulk vs. interface propensity of BrO^- . We accounted for polarization effects by rescaling the ionic charges. This convenient approach, which is suited for electronically homogeneous media, overestimates the anionic surface affinity in the air-liquid water case [4]. Even with that, Fig. 2 clearly demonstrates that the BrO^- density profile is depleted near the interface defined at the position where the water density drops to 50%, 22 Å. The MD results support the experimental findings: the hypobromite ion rarely visits the interface and remains predominately in the bulk. Preliminary results from first-principle MD also support the depletion of BrO^- from the interface obtained at classical MD level.

We acknowledge funding from the Swiss National Science Foundation (Grant 169176).

- [1] S. Wang et al., Proc. Natl. Acad. Sci., **112**, 9281-9286 (2015).
- [2] L. Artiglia et al., Nature. Comm., **8**, 700, 2017.
- [3] M. A. Brown et al., Rev. Sci. Instrum., **84**, 073904 (2013).
- [4] M. Vazdar et al., J. Phys. Chem. Lett., **3**, 2087-2091 (2012).

THE EFFECTS OF ORGANICS ON MULTIPHASE CHEMISTRY

J. Edebeli (PSI & ETHZ), M. Ammann, T. Bartels-Rausch (PSI)

We report on the reactive surface uptake of ozone (O_3) in a bromide (Br^-) and citric acid (CA) containing aqueous mixture. The goal is to better understand multiphase halogen chemistry in cold aerosol, snow, sea-ice or frost flowers.

The reaction of O_3 with halides is important in the lower troposphere due to the impact on the oxidation capacity and the fate of compounds in the atmosphere [1]. An important source of the condensed phase halides is sea-salt aerosol, which are often mixtures of organics and salts. The presence of organics in aqueous solutions is known to significantly alter their physicochemical properties such as viscosity and solubility of gases and ultimately their chemistry [2]. Therefore, we investigated the reaction of O_3 with Br^- in an acidic aqueous mixture containing sodium bromide (NaBr) and citric acid (CA) as proxy for the organic fraction of sea water derived brines in sea spray aerosol, snow or other cold environments.

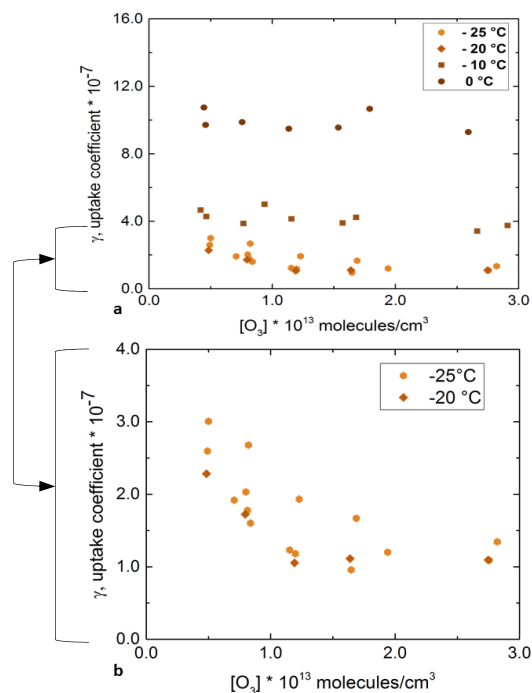


Fig. 1a, b. Plot of O_3 uptake coefficients, γ , as a function of ozone concentration ($[O_3]$) at different temperatures; Matrix: 1.3 M NaBr and 1.2 M citric acid equilibrated concentration; pH \sim 2. The bottom plot represents an expanded view of the data at -25°C and -20°C .

Fig. 1a shows the results of experiments conducted in flow tubes coated with a mixture of NaBr and CA at four temperatures (T , 0°C , -10°C , -20°C , -25°C). A decreasing trend of uptake coefficients (γ) with $[O_3]$ was observed at -20°C and -25°C (Fig. 1b). The decrease of γ indicates significant reactive uptake at low $[O_3]$ on the surface. The surface becomes saturated with

increasing $[O_3]$; hence, the leveling off of γ at high $[O_3]$, because the uptake coefficient is equivalent to the net reactive loss rate normalized to the gas kinetic collision rate. Such a trend in the reaction of O_3 with Br^- has previously been observed in absence of organics [3,4]. Oldridge and Abbatt interpreted the surface uptake as Langmuir-Hinshelwood type [3] as represented by equation 1. The uptake coefficient was invariant with $[O_3]$ at -10°C and 0°C (Fig. 1a). This and the level of the asymptotic limit at high ozone concentrations have been shown to indicate significant reactivity in the bulk [2].

The positive y-intercept from the linear fit to a plot of γ against $1/[O_3]$ gives the bulk uptake coefficient (Γ_{bulk}) of O_3 [3]. Subtracting Γ_{bulk} from γ gives Γ_{surf} . When equation 1 is re-written as equation 2, the Langmuir coefficient, K_{LangC} , can be obtained from the slope and y-intercept of a linear fit to the plot of $1/\Gamma_{\text{surf}}$ as a function of $[O_3]$.

$$\frac{1}{\Gamma_{\text{surf}}} = \frac{\omega\sigma}{4K_{\text{LangC}}k_s^{\text{II}}[\text{Br}^-]_s} + \frac{\omega\sigma K_{\text{LangC}}[O_3]_g}{4K_{\text{LangC}}k_s^{\text{II}}[\text{Br}^-]_s} \quad (1)$$

$$\frac{1}{\Gamma_{\text{surf}}} = A + AK_{\text{LangC}}[O_3]_g \quad (2)$$

Where ω = mean thermal velocity of ozone; σ = surface area occupied by an adsorbed O_3 molecule; $k_s^{\text{II}}[\text{Br}]_s$ = pseudo first order surface reaction rate. The calculated Langmuir coefficients were $1-3 \times 10^{-13}$ $\text{cm}^3/\text{molecule}$ at -20°C and -25°C . These estimates agree with that calculated by Oldridge and Abbatt, $\sim 10^{-13}$ $\text{cm}^3/\text{molecule}$ at -20°C [3]. The magnitude of Γ_{bulk} in this data-set (7×10^{-8}) compared to 1×10^{-8} without CA at -20°C [3] indicate that the CA increases the solubility of O_3 and/or the rate of Br oxidation. Thus, CA promotes the reactive bulk uptake in particular at warmer temperatures. This shows a significant effect of citric acid on the multiphase chemistry.

We could, only recently, directly observe an intermediate ozonide complex replacing the adsorbed precursor of the Langmuir-Hinshelwood mechanism [4]. Further analysis of this work in this direction is ongoing.

We acknowledge funding from the Swiss National Science Foundation (Grant 155999).

- [1] W. R. Simpson et al., Chem. Rev., **115**, 4035-4062 (2015).
- [2] M. Shiraiwa et al., P. Natl. Acad. Sci., **108**, 11003–11008 (2011)
- [3] N. W. Oldridge, N.W. et al., J. Phys. Chem. A, **115**, 2590-2598 (2011).
- [4] L. Artiglia et al., Nat. Comm., **8**, 700 (2017).

A CATIONIC SURFACTANT ACCELERATES BROMIDE OXIDATION

S. Chen, J. Edebeli (PSI & ETHZ), M. Ammann (PSI)

The reaction of ozone with sea-salt derived bromide is relevant for marine boundary layer chemistry. This study shows an obvious enhancement of ozone uptake to bromide solutions in presence of a cationic tetrabutylammonium surfactant.

The multiphase reaction of bromide with ozone is an important bromide oxidation pathway, which initiates the formation of molecular halogen compounds that later drive ozone depleting chemistry in the gas phase of marine air masses. The reaction of ozone with pure aqueous bromide solution exhibits an enhanced rate at the surface [1]. The ocean surface water and sea spray aerosol are enriched in organic compounds, which may have a significant effect on the way halide ions are distributed at the interface [2]. Tetrabutylammonium (TBA) has been selected for this study as a proxy for cationic surfactants deriving from biogenic oceanic material.

Solutions composed of a mixture of 0.1 M TBA bromide and 0.55 M NaCl, 0.1 M TBA bromide only, a mixture of 0.1 M NaBr and 0.55 M NaCl, and 0.1 M NaBr only, were used, respectively. TBA is expected to exhibit a surface excess of around 2.3×10^{14} molecule per cm^2 at 0.1 M [3]. The uptake coefficient of ozone (γ_{obs}) is derived from the observed fractional loss of ozone over a trough containing the aforementioned solutions and housed in a temperature controlled reactor. In equation 1, ω_{O_3} is the mean thermal velocity of the ozone molecules in the gas phase (cm s^{-1}), $[\text{O}_3, \text{bypass}]$ is the measured ozone concentration delivered to the reactor (measured with the reactor bypassed). $[\text{O}_3, \text{reactor}]$ is the ozone concentration downstream of the reactor. Q is the flow rate of the gas passing through the reactor ($\text{cm}^3 \text{s}^{-1}$). SA is the total surface area of the solution (cm^2).

$$\gamma_{\text{obs}} = \frac{4 \cdot Q}{\omega_{\text{O}_3} \cdot SA_{\text{reactor}}} \times \log \left(\frac{[\text{O}_3, \text{bypass}]}{[\text{O}_3, \text{reactor}]} \right) \quad (1)$$

Fig. 1 shows the measured ozone uptake coefficients at 277 K as a function of ozone concentration in the gas phase. At high ozone concentration (above 200 ppb), γ_{obs} is constant, whereas at low atmospherically relevant ozone concentration (between 30 and 100 ppb), γ_{obs} is decreasing. In previous studies [1,4], this behavior has been attributed to a surface reaction dominating at low ozone concentration. It results from the fact that the maximum coverage of O_3 on the surface is limited, which leads to the surface reaction rate saturating with higher ozone concentration. Because the uptake coefficient is the ratio of the reaction rate to the gas kinetic collision rate, the uptake coefficient related to the surface reaction decreases inversely with the gas

phase concentration of O_3 . This is not the case for the bulk phase reaction, since the bulk phase concentration of O_3 scales linearly with the gas phase concentration (Henry's law) in the relevant concentration range. The behavior of the uptake coefficient shown in Fig. 1 is the result of the combination of parallel reaction in the bulk (dominating at high ozone concentration) and reaction on the surface (dominating at low ozone concentration). The measured γ_{obs} in absence of TBA are consistent with previous studies from our group [1] and the work by Oldridge and Abbatt [4]. The difference between the pure NaBr and the mixed NaBr/NaCl solutions may be explained by the lower solubility of O_3 due to salting out by the 0.55 M NaCl. In presence of TBA, the ozone uptake coefficient is higher than on the pure NaBr and NaBr/NaCl mixed solutions at low ozone concentration, whereas they tend to be lower at high ozone concentration. In presence of TBA, the effect of 0.55 M NaCl seems not significant.

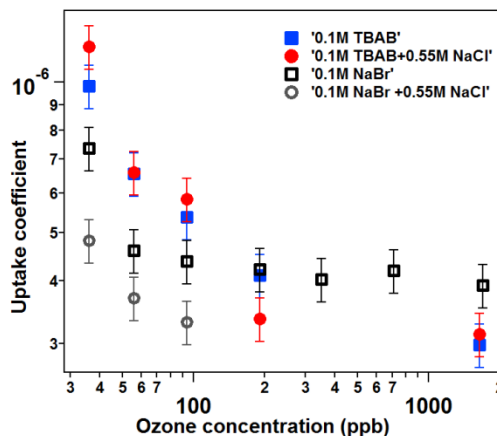


Fig. 1. Uptake coefficients of ozone as a function of ozone concentration in the gas phase.

It appears that the positively charged ammonium group in TBA helps to attract Br^- ions to the interface and possibly also leads to enhanced surface concentration of the $[\text{Br} \cdot \text{OOO}]^-$ intermediate that limits the reaction rate [1].

We acknowledge funding from the Swiss National Science Foundation (Grant 169176).

- [1] L. Artiglia et al., *Nat. Comm.*, **8**, 700 (2017).
- [2] M.-T. Lee et al., *J. Phys. Chem. A.*, **119**, 4600-4608 (2015).
- [3] J. Mata et al., *Coll. Surf. A*, **245**, 69-73 (2004).
- [4] N. Oldridge et al., *J. Phys. Chem. A*, **115**, 2590-2598 (2011).

WATER ADSORPTION ON GRAPHITE AT LOW TEMPERATURE

H. Yang (PSI & ETHZ), L. Artiglia, T. Bartels-Rausch, M. Ammann (PSI)

Electron yield near edge X-ray absorption fine structure (NEXAFS) spectroscopy is used to explore the hydrogen bonding structure of adsorbed water on graphite, a model system for deposition ice nucleation.

The nucleation of ice is an important process in chemistry, physics and atmospheric science. Although ice nucleation (IN) has been studied for a long time, our understanding of ice nucleation is still far from complete, particularly from a molecular point of view. Heterogeneous ice nucleation is likely controlled by subtle details of the way an IN active substrate modifies the hydrogen bonding structure of nearby water molecules by short and long range interactions. In this pilot study, the interactions between adsorbed water and graphite as a proxy for solid carbonaceous materials as substrate for deposition ice nucleation is investigated. The hydrogen bonding structure of H₂O is significantly different between liquid water and ice, which determines most of the differences in physical and chemical properties between the two phases. The difference between the hydrogen bonding structure of liquid water and ice can be experimentally observed by near edge X-ray absorption fine structure (NEXAFS) spectroscopy at the oxygen K-edge, because it involves resonant transitions into unoccupied molecular orbitals, which are very sensitive to the nearest neighbors of oxygen atoms. NEXAFS spectroscopy can be performed in electron yield mode, in which Auger electrons emitted upon initial core hole excitation are detected, which provides a surface sensitive NEXAFS spectrum. Experiments reported in this work were performed at the near ambient pressure photoelectron spectroscopy end station (NAPP) at the NANOXAS beamline at the Swiss Light Source (PSI, SLS).

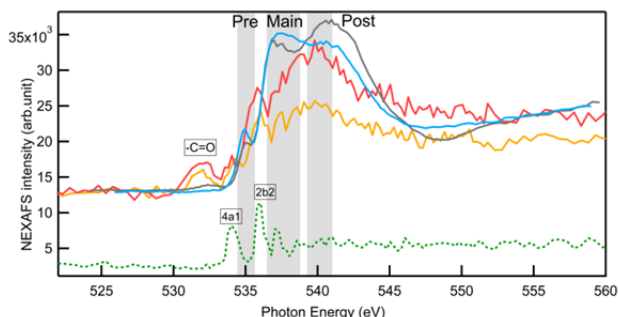


Fig. 1. Electron yield O K-edge NEXAFS spectra from highly oriented pyrolytic graphite (HOPG) in presence of water vapour at 0.5 mbar at a relative humidity of 60% at -22°C (orange) and 90% at -25°C (red). Spectra from liquid water (blue) and solid ice (black) and gas phase water (dotted green line) are also shown for comparison.

We have measured electron yield NEXAFS spectra of adsorbed water on a freshly cleaved highly oriented pyrolytic graphite (HOPG) surface under subsaturated conditions with respect to ice. Under isobaric conditions and by varying the temperature of the sample, we can change the local relative humidity, which leads to varying amounts of adsorbed water in equilibrium between the substrate and water vapor.

Fig. 1 shows the O K-edge NEXAFS spectrum of adsorbed water under different conditions of relative humidity, in comparison with the corresponding spectra of liquid water (measured with liquid jet XPS) and solid ice [1]. The absorption feature at 532 eV is due to -C=O groups on graphite or due to carbonyl contaminations on ice. This feature is absent in liquid water due to the cleaner surface of the liquid jet XPS experiment [2]. The pre-edge (535 eV) and main edge (537.5 eV) for liquid water is contributed by the weakly coordinated OH of hydrogen bonds in molecules with asymmetric donating H bonds, whereas strong H bonds between the two water molecules are contributing to the post edge peak (540 eV) [3,4]. These features (shaded area in Fig. 1) reflect the 2p character of the unoccupied valence orbitals at the site of the oxygen (O) atom of the water molecule. In comparison with liquid phase water, we note that the ice spectrum (black) shows a more intense post edge. This reflects that the hydrogen bonding network near the surface of hexagonal ice I_h is much more ordered than in liquid phase water [5]. The adsorption of H₂O on the HOPG surface causes an increase in the region around 540 eV, which is the post edge of the NEXAFS spectra. The preliminary analysis indicates that the spectrum of adsorbed water at 90% relative humidity (red) on HOPG resembles that of ice (black) in terms of post edge intensity, suggesting a highly ordered structure of the hydrogen bonding network of adsorbed water molecules under these conditions.

Future work will include studying water adsorption on kaolinite and other substrates known for their ability to induce ice nucleation.

We acknowledge funding from the Swiss National Science Foundation (Grant 169176).

- [1] X. Kong et al., *J. Phys. Chem. Lett.*, **8**, 4757–4762 (2017).
- [2] T. Bartels-Rausch et al., *ACS Earth and Space Chemistry* (2017).
- [3] S. Myneni et al., *J. Phys. Condens. Matter*, **14**, L213 (2002).
- [4] P. Wernet et al., *Science*, **304**, 995-999 (2004).
- [5] M. Leetmaa et al., *J. Electron. Spectrosc. Relat. Phenom.*, **117**, 135-157 (2010).

JANUS AT THE INTERFACIAL REGION OF ICE

A. Waldner (PSI & ETHZ), X. Kong, L. Artiglia, F. Orlando (PSI), T. Huthwelker (PSI/LSF), M. Ammann, T. Bartels-Rausch (PSI)

Dissociation of acids is one of the key concepts in chemistry. Here, we present a detailed picture of interfacial acid-base chemistry revealing distinct differences to that in the bulk phase.

Only recently, we have studied the adsorption of formic acid [1], a weak organic acid, and of the strong hydrochloric acid [2] to ice at 253 K. The core level spectroscopy data revealed a distinct behaviour of these two acids. Formic acid remained located within the upper 1 nm of the interfacial region at a surface coverage of a Langmuir monolayer. Fig. 1 shows a confirmation where we have extended the sampling depth compared to the previous experiments by using the tender X-ray range at the Phoenix beamline of the Swiss Light Source. In such experiments the sampling depth is given by the kinetic energy of the photoelectrons. The steep decrease of the calibrated carbon-to-oxygen photoemission intensity ratio with increasing photoelectron kinetic energy reveals that the presence of formic acid is restricted to the upper nanometre of the interface.

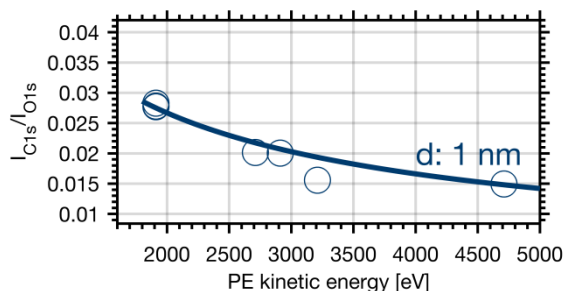


Fig. 1. Depth profile of formic acid at the air-ice interface. The photoemission intensity of carbon from formic acid (I_{C1s}) relative to that of oxygen from ice (I_{O1s}) is a direct measure of concentration. The larger the photoemission kinetic energy, the deeper is the interface being probed. The line represents results from a model fit giving the intensity ratio when the interfacial layer holding formic acid is 1 nm thick (d).

Hydrochloric acid was found within the upper 9 nm of the interfacial layer at a similar surface concentration and temperature [2]. The depth profiles of hydrochloric acid further showed the absence of dissociated acid in the upper nanometre of the surface. Obviously, the presence of hydrochloric acid deeper within the interfacial region went along with dissociation [2]. Accompanying X-ray absorption data, probing the structure of the hydrogen bonding network, revealed that the acidic anion present within the interfacial region forms solvation shells similar to those in bulk solution [1,3].

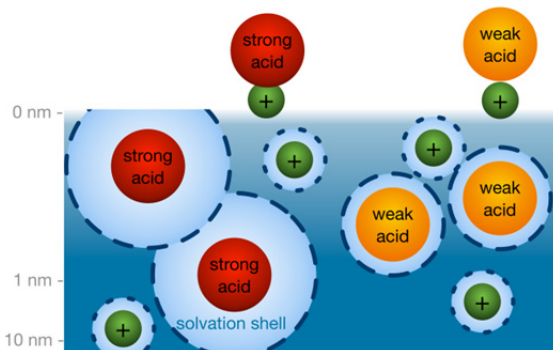


Fig. 2. The emerging picture of the chemical properties at the interfacial region of ice. Weak (orange sphere) and strong acids (red sphere) show two sides simultaneously: A molecular, physisorbed state and a dissociated form stabilized by solvation shells. Noteworthy, strong acids enter deeper into the interfacial region of ice than weaker ones, a consequence of a gradual loss of flexibility in the hydrogen-bonding network with depth.

We interpret these findings as co-existence of physisorbed molecular acid at the ice surface and of dissociated acid within the interfacial region. At temperatures where a quasi-liquid layer is present at the ice surface, the flexibility of the water molecules in this disordered hydrogen bonding network facilitates dissociation of acids. Consequently, dissociation seems not simply driven by the dissociation equilibrium in analogy to the liquid bulk phase, but rather a result of different chemical environments experienced by the adsorbed and by the solvated acid. Obviously, the depth into which acids enter the interfacial region is a consequence of the energy required to form solvation shells stabilizing the acidic anion. That strong acids with their significant dissociation energy enter deeper into the ice interfacial region indicates that it becomes more and more energy demanding to remove water molecules from an increasingly rigid hydrogen bonding structure.

We acknowledge funding from the Swiss National Science Foundation (Grant 149629) and the Swedish Research council (2014-6924).

- [1] T. Bartels-Rausch et al., ACS Earth & Space Chem., **1**, 572–579 (2017).
- [2] X. Kong et al., J. Phys. Chem. Lett., **8**, 4757–4762 (2017).
- [3] A. Krepelova et al., J. Phys. Chem. A, **117**, 401–409 (2013).

FOSTERING CHEMISTRY IN THE COLD

T. Bartels-Rausch (PSI), M. M. Frey (BAS), J. L. Thomas (LATMOS)

A new activity within the International Global Atmospheric Chemistry (IGAC) project co-sponsored by the Surface Ocean – Lower Atmosphere Study (SOLAS) focuses on natural processes specific to Earth's cold regions.

Both IGAC and SOLAS provide networks to bring international scientists across disciplines together. IGAC focuses on enhancing fundamental research of atmospheric chemistry processes. SOLAS focuses on processes at the ocean-atmosphere interface. They are both part of Future Earth and achieve their goals through sponsored activities. One new activity is CATCH, the Cryosphere and ATmospheric CHEmistry. Earth's cryosphere such as the Poles, the upper troposphere, and high mountain areas are an integral part of atmospheric chemistry.

CATCH aims to build a scientific network to facilitate atmospheric chemistry research within the international community with a focus on the chemistry, biology, and physics of the natural environment in cold regions. Two main objectives are 1) to foster future collaborative work by highlighting cross-disciplinary research questions and 2) to identify future research needs and opportunities. The interaction within and among the research communities will be established in workshops, and by holding sessions and events during international conferences.

CATCH held its first workshop in France in spring 2017. In total, 48 scientists from 14 countries from a wide range of disciplines and all career stages came together for two days to present their science related to CATCH in short talks or posters and to discuss ways of how to develop this new initiative. An on-going debate related to fundamentals in chemistry revolves around the nature of the air-ice interface and how it affects trace gas exchange and chemical reaction rates. Further, it became clear that the study of natural processes in the cold and polar regions is highly interdisciplinary, logistically challenging and expensive. It therefore relies heavily on international collaboration.

The next steps of CATCH will be to identify key research questions and build a platform and take action to address these, such as developing a white paper, scientific reviews, research proposals, a summer school, and coordinated field campaigns.



The cold and Polar regions are currently undergoing significant change with implications for regional and global climate, ecosystems, and society. CATCH science focuses on the following underlying natural chemical, biological and physical processes:

- How aerosols are formed and processed in cold regions;
- How cold region aerosols impact cloud properties;
- Feedbacks between climate change and atmospheric chemistry that are determined by changes in the cryosphere;
- How the ice core record can be used to understand global environmental change;
- How physical, chemical, biological, and ecological changes in sea ice and snow impact atmospheric chemistry;
- How microbiology adapts and impacts biogeochemical cycling of elements in ecosystems of cold environments;
- Understanding background composition (trace gases and aerosols) in cold regions that are undergoing industrialization and how they are impacted by climate change, including cryospheric change;
- Understanding the wider impacts of natural air-snow processes on climate and air quality linking the micro-scale with the regional and global scale;
- Studying how surface and fundamental chemical processes in ice depend on the state of the air-ice interface and how it affects release and uptake, as well as reaction rates of chemical species.

<http://www.igacproject.org/activities/CATCH>

We acknowledge funding from IGAC, SOLAS, and the French project PARCS.

PREFERENTIAL ELUTION OF MAJOR IONS IN SNOW AT THE WEISSFLUHJOCH

A. Eichler (PSI), J. Trachsel (WSL-SLF & ETHZ), S. E. Avak (PSI & Univ. Bern), S. Brüttsch (PSI), J. Edebeli (PSI & ETHZ), T. Bartels-Rausch (PSI), M. Schneebeli (WSL-SLF)

Major ion concentrations in the snowpack at Weissfluhjoch in the Swiss Alps are well preserved in the cold season. Meltwater percolation during warm periods causes preferential elution from the snowpack with Ca^{2+} and SO_4^{2-} being the most affected major ions.

The first fraction of meltwater from a melting snowpack usually contains a much higher concentration of solutes than the bulk snow [1]. This so-called "acid flush" in spring can have severe ecological effects on lakes and streams. Explaining the varying elution behaviour of different snow impurities and the relation to their microscopic location in snow and ice is one primary goal of the MiSo project [2].

Here we present the results of five sampling campaigns at the test site Weissfluhjoch (WFJ) in the Swiss Alps (2536 m a.s.l.) between January and June 2017, aiming at investigating impurity profiles in the snow cover during dry and wet conditions. Dry conditions prevailed for the first three sampling days (25.1, 22.2., 21.3.) (Fig. 1), partial melting occurred on 17.4., whereas the total snow profile was soaked with meltwater on 1.6. Snow height varied between 0.8 m (0.25 m water equivalent (w.eq.), 25.1.), 1.70 m (0.68 m w.eq., 17.4.), and 0.8 m (0.36 m w.eq., 1.6.). The snow profiles were sampled with a resolution of ~6 cm using pre-cleaned 50 ml PP tubes. A total of 108 samples were analyzed for major ions, water stable isotopes, and trace elements.



Fig. 1. Snow profile sampling at WFJ on 25.1.2017.

The records of selected major ions in the five snow pits are shown in Fig. 2. There is a good correspondence between the four snow profiles taken in winter and spring. On the contrary, meltwater disturbed the original records of certain major ions in the snow profile collected at the beginning of summer. Preferential elution of certain ions with respect to others was observed. Whereas NH_4^+ , Cl^- , and Na^+ were still preserved, NO_3^- , SO_4^{2-} , and Ca^{2+} were strongly depleted (Fig. 2). These findings match the results of our laboratory based elution experiments, where we exposed homogeneously

doped artificial and WFJ snow samples to well-defined metamorphism conditions and rinsed them with 0°C ultra pure water to determine the distribution of impurity concentrations between snow grain interior and surfaces [2,3]. Ca^{2+} and SO_4^{2-} were enriched at the snow grain boundaries during snow metamorphism, explaining their mobilisation with meltwater. Ions with a high solubility in ice such as NH_4^+ were embedded in the interior of the crystals and are thus less mobile.

The results of this sampling campaign indicate that atmospheric composition is well preserved in the major ion chemistry of the snowpack at WFJ during the cold season. Melt effects during the warm season lead to the preferential loss of several major ions from the snowpack depending on their microscopic location in snow and are especially pronounced for Ca^{2+} and SO_4^{2-} . Possible melt-effects on the trace element concentrations and water stable isotopes signal in the snowpack are currently under investigation.

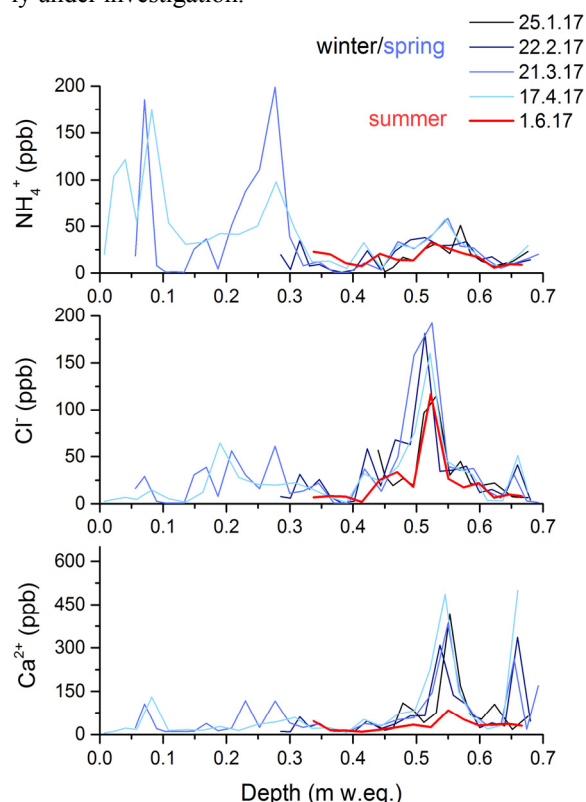


Fig. 2. Concentration records of Ca^{2+} , Cl^- , and NH_4^+ in five snowpits taken at the WFJ in winter/spring (black/blue) and summer (red).

We acknowledge funding from the Swiss National Science Foundation (Grant 155999)

- [1] S. Tsiouris et al., *J. Glac.*, **7**, 196 (1985).
- [2] <https://www.psi.ch/luc/miso>
- [3] J. Trachsel et al., this report, page 19.

REDISTRIBUTION OF MAJOR IONS DURING SNOW METAMORPHISM

J. Trachsel (WSL-SLF & ETHZ), S. E. Avak (PSI & Univ. Bern), J. Edebeli (PSI & ETHZ), M. Schneebeli (WSL-SLF), S. Brüttsch, T. Bartels-Rausch, A. Eichler (PSI)

The impact of snow metamorphism on the location of impurities in snow and its consequences for atmospheric chemistry is investigated within the MiSo project (Microscale Distribution of Impurities in SnOW and Glacier Ice), a cross-disciplinary project of the Paul Scherrer Institute and the WSL Institute for Snow and Avalanche Research.

The fate of different chemical impurities during snow metamorphism has strong consequences on snow and atmospheric chemistry and physics [1], but is little understood.

In this study we investigate the redistribution of major ions during snow metamorphism using a) homogeneously doped artificial snow and b) fresh snow from the Weissfluhjoch (WFJ) in the Swiss Alps (2843 m a.s.l.). Snow samples were exposed to a well-defined temperature gradient within a metamorphism chamber. Fig. 1 shows the structural evolution of the natural and artificial snow within the 60 days of the metamorphism experiment obtained with micro-computed tomography (μ CT). Although the structure of the initial snow samples varies, no difference is visible in the aged samples indicating the suitability of the artificial frozen droplets to mimic metamorphism of natural snow.

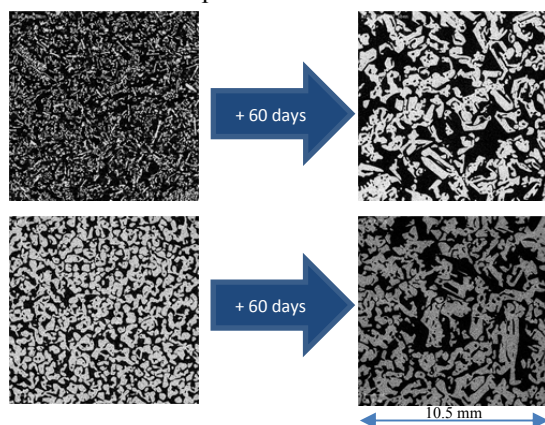


Fig. 1. μ CT scans of snow during dry metamorphism between 0 and 60 days using the same temperature gradient. Top: structural development of natural WFJ snow; bottom: artificial droplets.

Snow samples were taken out of the metamorphism chamber after 1, 3, 6, 12, 30, and 60 days, leached 10 times with 0°C ultrapure water and the remaining snow was molten. In the 10 eluates and the snow residual concentrations of Na^+ , NH_4^+ , Ca^{2+} , Cl^- , F^- , and SO_4^{2-} were analysed. Whereas ion concentrations in the first eluates characterize the composition at grain boundaries, those of the snow residuals represent conditions in the snow grain interiors.

The results of the elution experiments show a strong enrichment of certain ions in the snow grain interiors with time (Fig. 2). Highest enrichments were observed for NH_4^+ and Cl^- (artificial snow) and F^- and NH_4^+ (nat-

ural snow). These results are in agreement with the high solubility of NH_4^+ , F^- , and Cl^- in ice [2], leading to an incorporation of these species into the ice lattice during snow metamorphism. In contrast, the highest concentrations at grain boundaries were observed for Ca^{2+} and SO_4^{2-} (artificial snow, [3]) and Na^+ , Ca^{2+} , and SO_4^{2-} (natural snow) (measured in the first of the 10 eluates) in accordance with a lower solubility in ice.

The differences in the burial of major ions during metamorphism between artificial and natural snow are not primarily due to structural differences between the two types of snow, since initial differences disappear after a few days. We assume that concentration differences play a major role. Whereas concentrations of SO_4^{2-} and NH_4^+ are similar, F^- , Cl^- , Na^+ , and Ca^{2+} concentrations are much lower in the natural snow. The dependence of impurity burial during snow metamorphism on concentrations of chemical species is subject of a current investigation [4].

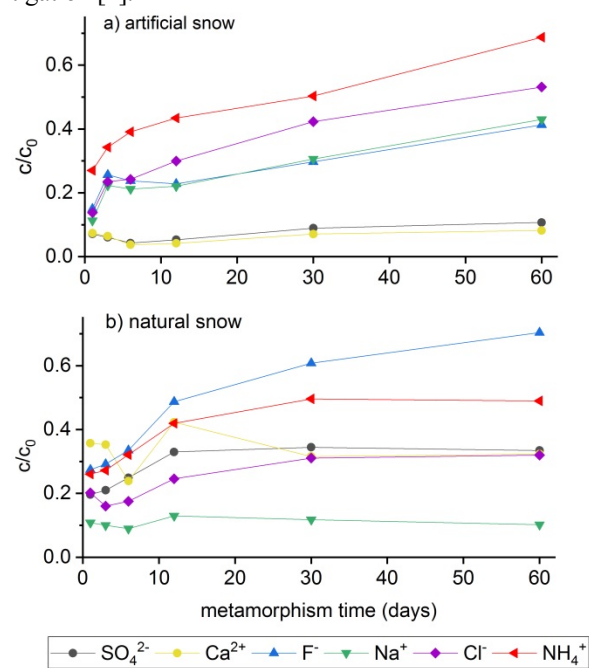


Fig. 2. Evolution of the ion concentrations in the snow grain interiors (residual snow) after 1, 3, 6, 12, 30, and 60 days of metamorphism, a) artificial snow, b) natural snow.

We acknowledge funding from the Swiss National Science Foundation (Grant 155999).

- [1] T. Bartels-Rausch et al., *Atmos. Chem. Phys.*, **14**, 1587-1633 (2014).
- [2] A. Eichler et al., *Tellus*, **53B**, 192-204 (2001).
- [3] J. Trachsel et al., *Annual Report Lab. of Environm. Chem. PSI*, **15** (2016).
- [4] S. Avak et al., this report, page 20.

IMPACT OF MELTWATER ON ICE CORE TRACE ELEMENT RECORDS

S. E. Avak, M. Schwikowski (PSI & Univ. Bern), A. Eichler (PSI)

The firm part of a high-alpine ice core from upper Grenzgletscher, southern Swiss Alps, was shown to be affected by an inflow and subsequent percolation of meltwater. We acquired concentration profiles of 35 trace elements to characterize the impact of meltwater percolation and the implications it has regarding their microscopic location and their potential as environmental proxies.

Past atmospheric pollution can be reconstructed from high-mountain glacier ice core trace element records. Due to the current global temperature increase glaciers at high altitudes are in danger to experience melt, strongly altering the information stored in these environmental archives. We studied the behaviour of anthropogenic, dust and volcanic related trace elements by analysing a 50 m segment of the Grenzgletscher ice core including a 13 m section affected by a limited amount of meltwater percolation [1]. Some trace elements revealed a significant depletion in concentration whereas others were well preserved as indicated by the presence of seasonal variability (Fig. 1).

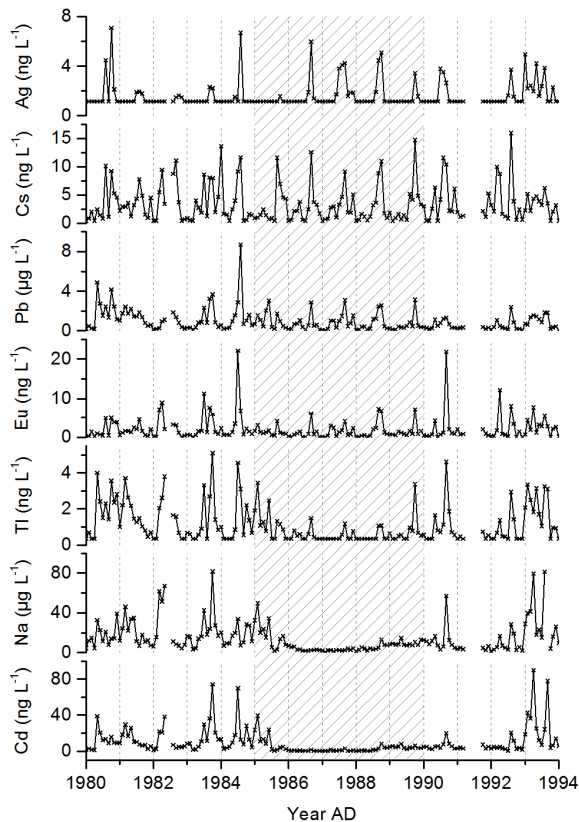


Fig. 1. Exemplary concentration records of Ag, Cs, Pb, Eu, Tl, Na, and Cd of the Grenzgletscher ice core segment. The shaded area (1985–89) indicates the section affected by an inflow and subsequent percolation of meltwater.

We suggest that this fractionation of trace elements with respect to meltwater percolation (Fig. 2) is a result of their microscopic location in the ice structure, i.e. segregation to grain surfaces versus incorporation into the lattice. No dependence between the fractionation and the size of the investigated trace elements could be found, whereas atmospheric concentration levels are a major driving force determining their segregation or incorporation. Abundant elements such as Ca, Mg, Mn, Na, and Zn seem to be segregated to grain boundaries, prone to meltwater relocation. Rare elements including Ag, Bi, Cs, La, Sb, and W are rather incorporated into the ice lattice, indicated by their strong preservation (Fig. 2). Based on their distinct retention, we propose that in particular Ag, Al, Bi, Cu, Cs, Fe, Pb, Sb, W, and the rare earth elements might serve as robust environmental proxies in ice core records from glaciers partially affected by melting.

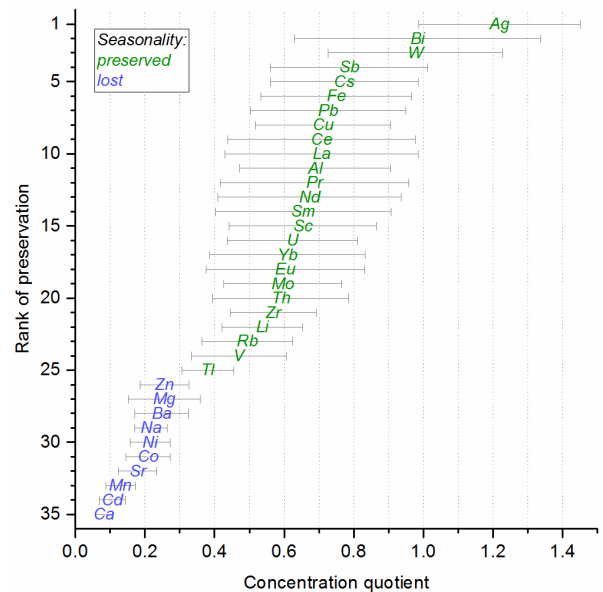


Fig. 2. Rank of preservation against the concentration quotient defined as the mean concentration ratio between the section disturbed by meltwater percolation (1986–88) and the remaining two unaffected parts of the ice core segment (1980–84 and 1990–92) of a specific trace element. Colour coding indicates how the seasonal pattern is reflected within the section affected by meltwater percolation.

We acknowledge funding from the Swiss National Science Foundation (Grant 155999).

[1] A. Eichler et al., *Tellus*, **53B**, 192-203 (2001).

EFFECT OF LIGHT-ABSORBING IMPURITIES ON GLACIER ALBEDO

A. Dal Farra (PSI & Univ. Bern), A. Marinoni (Univ. Pavia), K. Naegeli (Univ. Aberystwyth), M. Schwikowski (PSI & Univ. Bern)

Assessing the role of light absorbing impurities in lowering glacier albedo and consequently in advancing glacier melt is crucial to project the future fate of glaciers.

Light-absorbing impurities (LAI) are known to considerably influence glacier melt [1], accelerating the current trend of negative mass balance in the case of many glaciers, including Glacier de la Plaine Morte [2]. The magnitude of the LAI's effect depends on their abundance on the glacier surface as well as on their optical properties. LAI are divided into three classes (black carbon (BC), organic matter, and mineral dust). An average relative abundance of 91.1, 8 and 0.9% was determined for mineral dust, organic matter and BC, respectively, with a thermo-optical OC/EC analyzer (Model4L, Sunset Laboratory Inc., USA) in 110 surface samples collected on Glacier de la Plaine Morte. The spatial distribution of the LAI classes revealed that mineral dust and organic matter are mostly of local origin (Fig. 1), which was confirmed for the mineral dust by its composition determined with X-ray diffractometry (XRD, XPertPro, MPD Panalytical): quartz, plagioclase, K-feldspar, calcite, amphibole and dolomite.

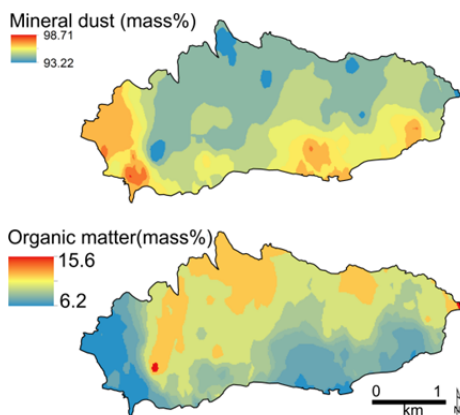


Fig. 1. Distribution of mineral dust (top) and organic matter (bottom) on Glacier de la Plaine Morte as determined by interpolation of 110 data points.

With a novel method, using a hyperspectral imaging microscope spectrometer (HIMS) the reflectance spectrum of each LAI class was determined averaging 10 to 15 measurements of different particles belonging to mineral dust, organic matter and BC (Fig. 2). These characteristic reflectance spectra along with that of bare ice were used as endmembers in the spectral unmixing of reflectance spectra measured on the glacier with a field spectroradiometer (FieldSpec 3, ASD Inc., PANalytical).

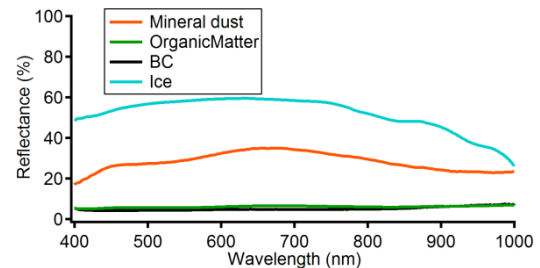


Fig. 2. Characteristic reflectance spectra of mineral dust, organic matter and BC collected with the HIMS and a spectrum of bare ice collected with the field spectroradiometer.

The relative abundance determined with this method matched well with the measured values for the area where the spectra were collected (with a 0.4% average standard deviation). The same spectral unmixing was applied on a highly spatially resolved airborne hyperspectral dataset (APEX – Airborne Prism EXperiment), covering the entire glacier surface. The overall relative abundance obtained from the spectral unmixing of all the spectra from the airborne dataset is 91.6, 4.9 and 3.3% for mineral dust, organic matter and BC, respectively; values which are comparable with the measured average (91.1, 8 and 0.9%). The resulting distribution (Fig. 3) of the LAI on the glacier and the average relative abundance values agreed well with the interpolation of the 110 samples measured. Relatively high abundance of organic matter in the areas with particularly low albedo suggests that the latter plays an important role in glacier darkening.

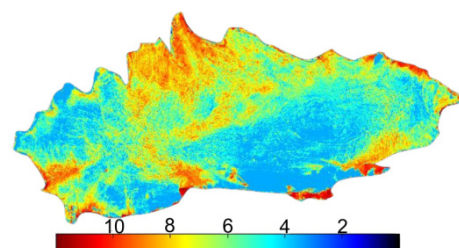


Fig. 3: Organic matter distribution on the glacier as determined by the spectral unmixing of the APEX spectral data.

We acknowledge support from Dr. Chiara Uglietti, Dr. Urs Eggenberger and all the fieldwork team.

- [1] C. E. Boggild et al., *J. Glac.*, **56**, 101 (2010).
- [2] K. Naegeli et al., *Rem. Sen. Envir.*, **168**, 388 (2015).

NOT GUILTY – THE CASE INDUSTRIAL SOOT VS. ALPINE GLACIER RETREAT

M. Sigl, T. M. Jenk (PSI), D. Osmont (PSI & Univ. Bern), N. J. Abram (ANU), J. Gabrieli (Univ. Venice), M. Schwikowski (PSI & Univ. Bern)

The fast retreat of Alpine glaciers since the mid-19th century documented in photographs and paintings is a signature symbol for the human impact on global climate – yet, the key driving forces remain elusive. Here we argue that not industrial soot but volcanic eruptions were responsible for the apparently accelerated deglaciation starting in the 1850s.

This year’s summer excursion led the Laboratory of Environmental Chemistry (LUC) to the Rhône glacier. Situated in the Valais, this glacier covers today 23% less area compared to 1850 AD (Fig. 1). Understanding the drivers of the exceptionally fast glacier change following the Little Ice Age (LIA) maximum is of eminent importance for an improved understanding of glacier sensitivity in the past and at present, as well as and for future glacier projections. Attribution of changes in the cryosphere to anthropogenic emissions of greenhouse gases and radiative effective aerosols such as sulfate and industrial black carbon (BC) or soot [1], however, requires a detailed understanding of the transient evolution of these forcing agents from pre-industrial to present-day. Equally important is to bound the role of natural forcing (e.g. volcanism) in promoting glacier growth and or retreat.



Fig. 1. The Rhône glacier and other mountain glaciers retreated rapidly from their 19th century maximum. Credit: ETH-Bibliothek of ETH Zurich under the creative commons CC-BY-SA license.

Using a state-of-the-art ice-core BC reconstruction from Colle Gnifetti in the Alps, high-resolution observational glacier length records [2], and an improved time series of stratospheric aerosol optical depth resulting from explosive volcanism [3] we show that the variability of glacier front positions throughout the 19th and early 20th century was strongly driven by large volcanic eruptions (Fig. 2). Periods of extended glacier lengths (i.e. 1820s, 1840s, 1880s) consistently followed periods with clusters of large stratospheric eruptions promoting cold and wet summers in the Alps plausible enforced by a strong albedo feedback resulting from widespread snow cover. Volcanically quiescent time periods (i.e. 1850-1880) allowed glacier terminus positions to retreat throughout the Alps.

The “time-of-emergence” [4] of significant industrial BC deposition on Alpine glaciers during the industrialization in Central Europe, however, has not occurred

before 1875 \pm 7 AD. At this time, glaciers in the Western Alps had on average already experienced 82% (52-92%, 2 σ) of their total mid-19th century cumulative length reduction (Fig. 2). These findings support a negligible role of snow albedo radiative effects in forcing glacier recession at the end of the LIA, contradicting previous model-based studies which were lacking such strong observational constraints [1]. Our study highlights the importance of volcanic eruptions in prompting past glacier advances in the Alps, providing necessary constraints for more realistic projections of Alpine glaciers in the future.

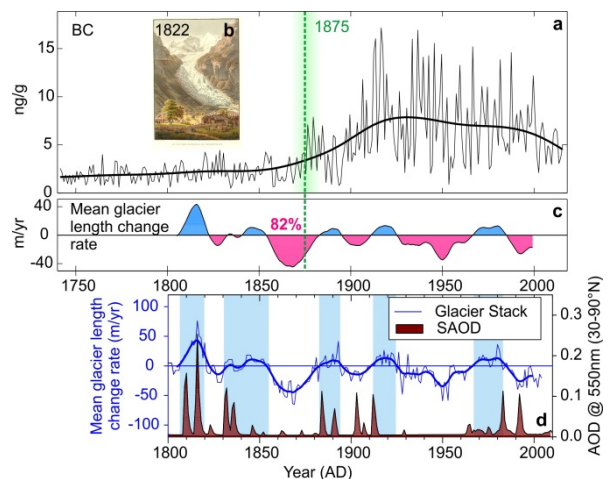


Fig. 2. **a)** Colle Gnifetti BC concentrations (black) and estimated “time-of-emergence” (green) of industrial BC deposition from its natural background variability; **b)** Unterer Grindelwaldgletscher in 1822 (Gabriel Lory) used together with three other glaciers to determine **c)** mean glacier length change rate during widespread advance (blue shading) and retreat phases (red shading); **d)** stratospheric aerosol optical depth from volcanic eruptions and mean annual (decadal, thick line) glacier length variability since 1800 AD.

We acknowledge funding from the Swiss National Science Foundation (Grant 154450).

- [1] T. H. Painter et al., Proc. Natl. Acad. Sci. USA, **110**, 15216-15221 (2012).
- [2] S. U. Nussbaumer & H. J. Zumbühl, Clim. Change., **111**, 301-334 (2012).
- [3] M. Toohey & M. Sigl, Earth Syst. Sci. Data, **9**, 809-831 (2017).
- [4] E. Hawkin & R. Sutton, Geophys. Res. Lett., **39**, L01702 (2012).

BIOMASS BURNING EMISSIONS OBSERVED AT JUNGFRAUJOCH

D. Osmont (PSI & Univ. Bern), M. Sigl (PSI), S. O. Brügger (Univ. Bern), R. Modini (PSI/LAC), M. Schwikowski (PSI & Univ. Bern)

Carbonaceous particle emissions from outstanding forest fire events in Portugal in June 2017 were detected at Jungfraujoch, Swiss Alps, in both the atmosphere and the snowpack.

In recent years, the occurrence of devastating wildfires has increased in many regions, leading to substantial socioeconomic and environmental consequences [1]. Portugal is a country severely affected by recurrent forest fire events. On 17 June 2017, lightning ignited the forest near Pedrogao Grande, and the resulting fire rapidly spread, killing 65 people, burning more than 30'000 ha, and emitting a huge plume of smoke that travelled for four days before reaching Switzerland. On 21 June, the MeteoSwiss lidar in Payerne detected a layer of smoke between 3000 and 5000 m a.s.l corresponding to the arrival of the plume, which intensified on 22 June and whose origin was confirmed by back-trajectory analysis. This layer of smoke became visible on the Jungfraujoch (JFJ) webcam, 3450 m a.s.l in the Bernese Alps, on 22 June in the morning, when a peak of equivalent black carbon (eBC) was detected at the JFJ (Fig. 1), with values several times as high as the background conditions. Significant snowfalls then occurred at JFJ on 25, 26, 28 and 29 June and snow samples were collected from a pit on 30 June.

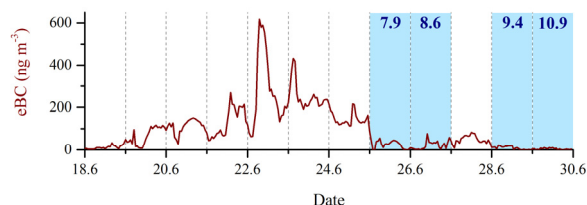


Fig. 1. JFJ atmospheric eBC concentration. Days with snowfall are highlighted in blue, with the associated amount in cm, inferred from precipitation data from Lauterbrunnen, assuming a snow density of 0.2 g cm^{-3} .

The snowpit depth was 1.10 m. Snow morphology and density were determined. 20 samples and 20 replicates were taken for refractory black carbon (rBC) and major ions analysis at 5 cm resolution. 6 samples were taken for microscopic charcoal ($> 10 \mu\text{m}$) analysis, at 10 cm resolution between 20 and 80 cm depth. rBC was measured by a Single Particle Soot Photometer (SP2), major ions by ion chromatography and charcoal by optical counting. The snowpit profile (Fig. 2) shows low density snow in the upper 22 cm, reflecting the latest snowfalls on June 28–29, and denser snow between 22 and 50 cm depth, roughly corresponding to the snowfalls on June 25–26. Below 50 cm, exact dating becomes impossible, but the presence of ice lenses and more compact snow indicates older snow which experienced the heat wave lasting until June 24th.

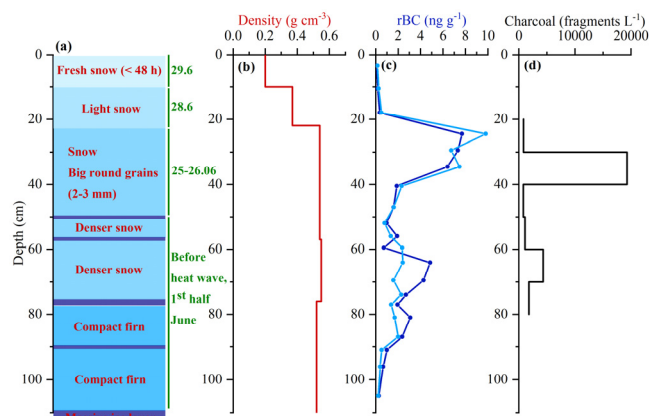


Fig. 2. a) Snowpit stratigraphy (ice lenses in dark blue), b) density profile, c) rBC profile (replicates in light blue) and d) charcoal profile.

A strong rBC peak is visible in the snow profile between 22 and 37 cm, with concentrations as high as 10 ng g^{-1} (Fig. 2), while the very fresh snow almost does not contain any rBC. This trend is well reproduced by the replicates ($r = 0.90$). The mode of the rBC mass size distribution (constantly around 300 nm) suggests a biomass burning origin. This is corroborated by very high charcoal concentrations at the same depth, but other fire tracers such as ammonium or formate do not display correspondingly high values. The atmospheric eBC concentrations reveal that most of the plume travelled over Switzerland on 22 June and that concentrations were already lower in the next two days before returning to background values on 25 June. We therefore hypothesize that the snowfalls on 25 June scavenge the remaining atmospheric BC leading to the peak values in snow. The thinner charcoal peak could indicate that wet scavenging occurs more rapidly for charcoal due to its larger size. Wet deposition seems to be the preferential pathway as the peak is spread over the whole accumulated snow layer while dry deposition would rather create a thin and unique highly concentrated layer. As no precipitation occurred on 22 June, the highest atmospheric concentrations were not archived in the snowpack. rBC wet scavenging ratios W , defined as $W = \rho C_s / C_a$, with ρ the air density in g m^{-3} , C_s the concentration in snow in ng g^{-1} and C_a the concentration in air in ng m^{-3} , were calculated. First estimations, after applying a correction factor of 2.7 between rBC and EBC concentrations, are 71 (110) for low (high) atmospheric BC burden, respectively.

We acknowledge funding from the Swiss National Science Foundation (Grant 154450).

[1] M. A. Moritz et al., *Nature*, **515**, 58–66 (2014).

HOLOCENE BIOMASS BURNING TREND INFERRED FROM AN ANDEAN ICE CORE

D. Osmont (PSI & Univ. Bern), M. Sigl (PSI), M. Schwikowski (PSI & Univ. Bern)

We present the first Andean black carbon ice-core record, retrieved from Illimani glacier and spanning the entire Holocene, allowing us to reconstruct past biomass burning trends in the Amazon Basin.

The tropical Andes are of prime interest as they host most of the low-latitude glaciers in the world, acting as invaluable archives of tropical climate and atmosphere. Their proximity to the Amazon Basin, one of the major contributors to global biomass burning emissions, makes Andean ice cores suitable to reconstruct paleofire trends in South America and improve our understanding of the complex linkages between fires, climate and humans. In this respect, black carbon (BC), produced by the incomplete combustion of biomass and fossil fuel, can be used as a suitable proxy.

Here, we present the first black carbon ice-core record from the Andes, derived from two ice cores recovered at 6300 m a.s.l from Illimani glacier in the Bolivian Andes. At this site located on the eastern side of the Andes, moisture mainly originates from the Amazon Basin (and ultimately the Atlantic Ocean) [1]. A 138 m long ice core was retrieved in 1999, spanning the entire Holocene back to the last deglaciation 13000 years ago, with a mean annual net accumulation of 0.58 m water equivalent (weq) [1]. In addition, a 25 m long shallow firn core was extracted in 2015, covering the time period 1995-2015, with a mean annual net accumulation of 0.72 m weq. The two ice cores were processed at PSI and the resulting 3820 samples were analyzed for BC with a Single Particle Soot Photometer (SP2) according to [2].

The BC record displays a strong seasonality, with high values during the cold and dry season corresponding to the austral winter (April-October) and low values in the wet and warmer austral summer (November-March). This seasonality is also present in trace element or ion records such as calcium or ammonium, suggesting it to be primarily driven by common transport and deposition processes. However, biomass burning emissions from the Amazon Basin are also expected to contribute substantially to the BC deposited at Illimani during the dry season, when the fire season peaks.

The study of BC long-term trends documents changes in emission sources or transport patterns (Fig. 1). They closely follow regional climatic variations during the Holocene, similarly to the ammonium record which was thought to be a temperature proxy reflecting biogenic emissions from the Amazon Basin [1]. Higher BC concentrations are visible during dry and warm periods such as the Holocene Climatic Optimum (6500-3500 BC) and the Medieval Warm Period (1100-1400 AD). Lower BC concentrations are rec-

orded during cold and wet periods like the last deglaciation (11000-9000 BC) and the Little Ice Age, particularly between 1700 and 1800 AD. Sharp variations around 6500-6000 BC could be related to the climatic reversal induced by the 8.2 ka event. Contrary to most of the Northern Hemisphere ice cores, no strong anthropogenic contribution can be seen in the 20th century, potentially because of the high altitude of the drill-site and its remoteness from major source regions. The two-fold increase in BC concentrations since 1870 could result from rising temperatures responsible for enhanced biomass burning in the Amazon Basin.

Such long-term trends are corroborated by other studies suggesting drier conditions over the Bolivian Altiplano during the Holocene Climatic Optimum [3] and elevated fire activity in the Bolivian Amazonian lowlands [4,5]. Except for the 20th century, a similar temporal variability is observed in a BC ice-core record from Antarctica, for which South America biomass burning is assumed to be the dominant source [6].

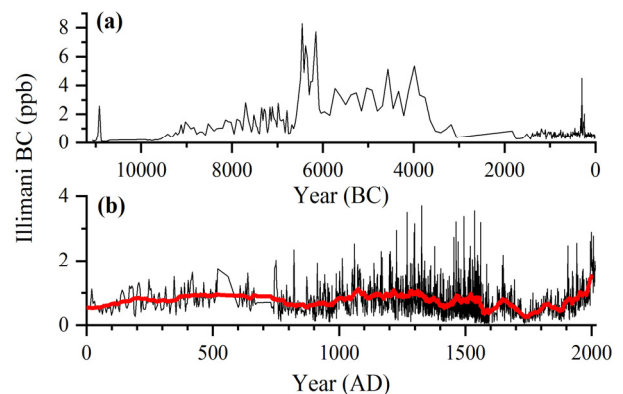


Fig. 1. Illimani BC record spanning a) 11000-0 BC, b) 0-2015 AD (black line: annual averages after 1639, raw data before; red line: 31-point moving average).

We acknowledge funding from the Swiss National Science Foundation (Sinergia: Paleo fires from high-alpine ice cores 154450).

- [1] T. Kellerhals et al., *J. Geophys. Res.*, **115**, D16123 (2010).
- [2] I. A. Wendl et al., *Atmos. Meas. Tech.*, **7**, 2667-2681 (2014).
- [3] P. A. Baker et al., *Science*, **291**, 640-643 (2001).
- [4] S. O. Brugger et al., *Quat. Sci. Rev.*, **132**, 114-128 (2015).
- [5] M. J. Power et al., *Phil. Trans. B*, **371** (2001).
- [6] M. M. Arienzo et al., *J. Geophys. Res. Atmos.*, **122**, 6713-6728 (2017).

EXTRACTION SYSTEM FOR DISSOLVED ORGANIC CARBON IN GLACIER ICE

L. Fang, J. Schindler (PSI & Univ. Bern), T. M. Jenk (PSI), M. Schwikowski (PSI & Univ. Bern)

Dating of ice cores from high alpine glaciers is challenging due to limited glacier thickness, resulting in strong annual layer thinning near bedrock. To investigate the suitability of ^{14}C dating on Dissolved Organic Carbon (DOC), we develop a low blank and high efficient extraction system for glacier ice.

The extraction method in brief: Ice samples after cutting and rinsing with ultrapure water are melted under helium gas in a melting vessel. Water insoluble organic carbon and elemental carbon are separated by filtration and inorganic carbon is removed via acidifying and degassing with helium. The remaining DOC in the solution is oxidized by UV lamps. Produced CO_2 is quantified manometrically after cryogenic trapping and sampled to glass vials for ^{14}C analyses. The oxidation blank, $0.9 \pm 0.2 \mu\text{gC}$, is calculated through irradiation of ^{14}C standards in the pre-cleaned system (Fig. 1). The total blank is slightly higher with about $1.3 \pm 1.4 \mu\text{gC}$ ($n=21$) using ultrapure water ice, with the variability probably resulting from changing water quality.

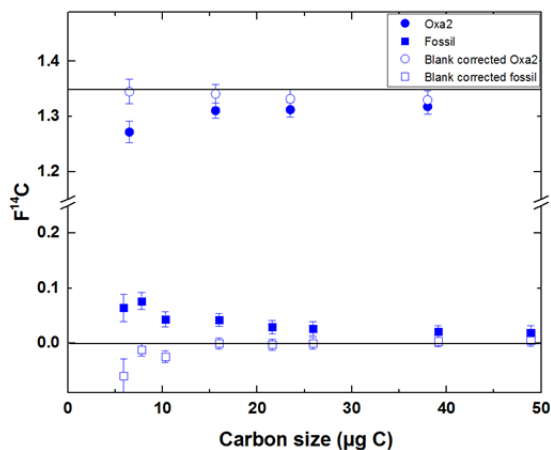


Fig. 1.

1. $F^{14}\text{C}$ of radiocarbon standards. Two horizontal line are Fossil $F^{14}\text{C}=0$ and Oxa2 $F^{14}\text{C}=1.34033$.

With the fixed oxidation time of 45 min of the original setup, average oxidation efficiencies of 82%, 105%, 79% and 54% for oxalate, formate, phthalate and acetate were observed, respectively (Fig. 2a). In order to obtain higher recovery, we modified the setup by installing a CO_2 detector inline. This increased our recovery up to $90 \pm 6\%$ (without phthalate) through extending the oxidation time until CO_2 is no longer formed (Fig. 2b). Unfortunately, this resulted in much longer oxidation times. Based on the study of photo-assisted Fenton type processes for the degradation of phenol [1], we used Fe^{2+} and H_2O_2 to facilitate oxidation. 2 ml of 100 ppm FeSO_4 and 1 ml of H_2O_2 solution were added to the reactor at the beginning of the pre-cleaning step. Another 1 ml of H_2O_2 solution was injected into the sample right before the UV irradiation. The average oxidation efficiency is significantly improved to $96 \pm 6\%$ for all the standards (Fig. 2c).

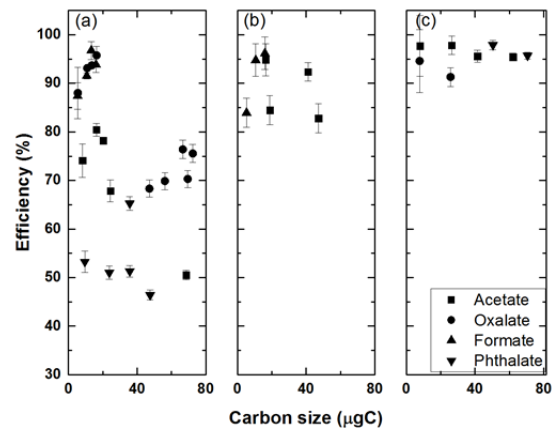


Fig. 2. Oxidation efficiency. (a) original setup with fixed oxidation time at 45 min ; (b) modified setup ; (c) modified setup with Fe^{2+} and H_2O_2 .

We applied our setup to extract DOC from the 43 m long Piz Zupò firn core recovered in 2002, which was well dated by annual layer counting. A high mean annual accumulation rate of $2.6 \pm 0.8 \text{ m w.e.}$ [2] allows investigating the seasonal variation of DOC. However, the DOC concentrations show no clear seasonal trend, and an extremely high DOC concentration of $1407 \pm 114 \text{ ppb}$ was observed at the top part of this core. These high concentrations and depleted ^{14}C values suggested this core has been contaminated. Accordingly, DOC concentrations show significant increase with decreasing density of the firn (Fig. 3).

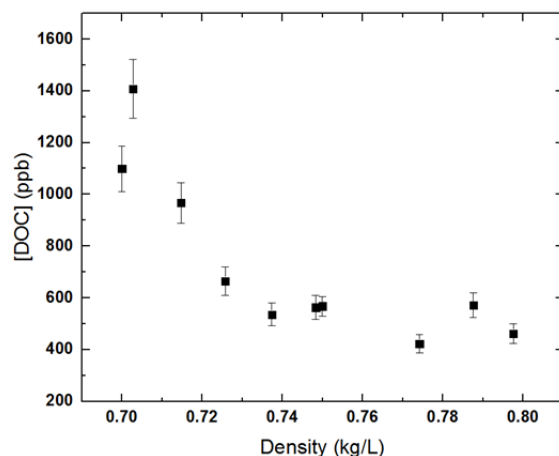


Fig. 3. DOC concentrations versus firn density.

We acknowledge support from Sönke Szidat and the Laboratory for the Analysis of Radiocarbon with AMS (LARA).

- [1] H. Kušić et al., *J. Hazardous Materials*, **136.3** 632-644 (2006).
- [2] H. Sodemann et al., *Atmos. Chem. Phys.*, **6.3**, 667-688 (2006).

^{14}C IN DISSOLVED ORGANIC CARBON (DOC) IN THE FIESCHERHORN ICE CORE

L. Fang (PSI & Univ. Bern), T. M. Jenk (PSI), M. Schwikowski (PSI & Univ. Bern)

Glaciers are valuable archives for reconstructing pre-industrial to industrial changes of DOC. Combining DOC concentrations with ^{14}C analyses, we can estimate the biogenic and anthropogenic contributions to atmospheric DOC through time.

We used our new DOC extraction setup which is characterised by a low total blank of $1.3 \pm 1.4 \mu\text{gC}$ ($n=21$) and a high average oxidation efficiency of $96 \pm 6\%$ to analyse samples from the Fiescherhorn ice core collected in 2002 [1]. This ice core is 150.5 m long and well dated back to 1682 by annual layer counting. The average DOC concentration for the time period 1680-1750 and 1890-1940 is 79 ± 27 ppb, which is comparable with previously reported alpine DOC concentrations [2]. DOC concentrations do not significantly vary with time, except for one elevated value of 173 ± 18 ppb in the period 1896-1899. There is no increase due to anthropogenic emissions from coal burning, which is surprising, but consistent with the absence of clear long-term trends in the concentrations of formate, ammonium (Fig. 1), and water insoluble organic carbon (WIOC, not shown, [1]). Also in the Mt. Blanc ice core DOC concentrations started to increase only after 1950 [2]. This agreement suggests that DOC has been well preserved in the ice core, which was collected 17 years ago. Compared to WIOC, DOC concentrations are a factor of 2-3 higher, which is comparable with the ratio in the Mt. Blanc ice core [2].

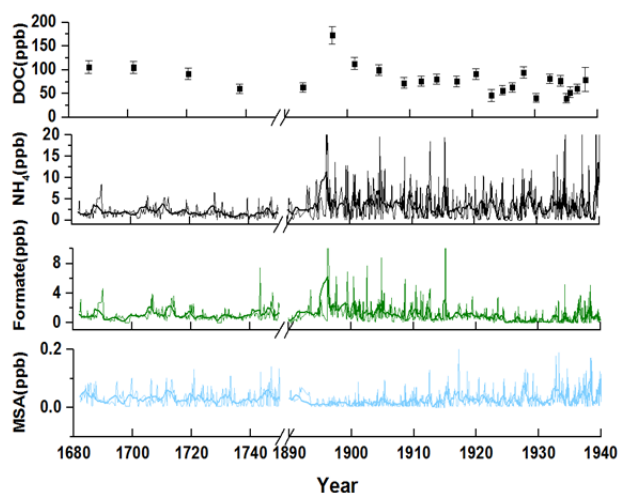


Fig. 1. DOC, ammonium (NH_4^+), formate (HCOO^-), and methanesulfonate (MSA) concentrations in the Fiescherhorn ice core.

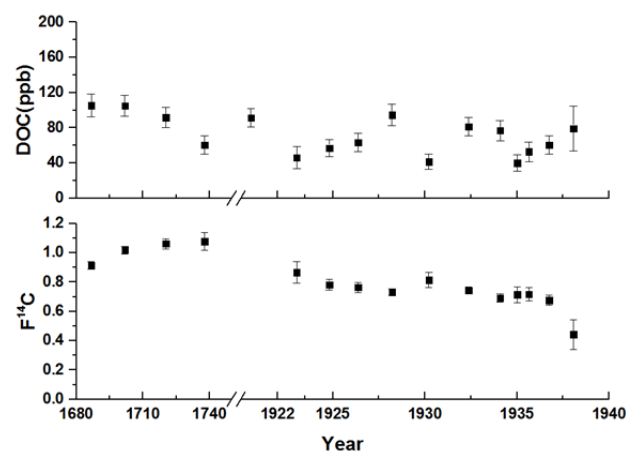


Fig. 2. F^{14}C of DOC in the Fiescherhorn ice core.

Nevertheless, radiocarbon analyses of DOC indicate significant anthropogenic modification to atmospheric DOC even though not visible in the concentrations. High F^{14}C values of 1.02 ± 0.04 ($n=4$) were observed in pre-industrial period (1680-1740). These values close to 1 indicate that DOC before the industrial revolution was of pure biogenic origin. F^{14}C values of DOC decreased significantly from 0.87 to 0.44 during the period of 1920 to 1940, which implies increased anthropogenic contributions to atmospheric DOC. More than 30% of DOC originated from fossil combustion between 1936 and 1938, which is comparable with the anthropogenic contribution to WIOC in this ice core [1].

The pre-industrial (1680–1740) average F^{14}C value of 1.02 ± 0.04 results in a one-sigma age range of modern to 286 cal BP (2002-1664), with the most likely values (since we know the samples cannot be modern) and 40% probability ranging from 162-286 cal BP (1664-1788), which is in reasonable agreement with the age obtained by annual layer counting.

Future work includes further DO^{14}C analyses to close the gaps in the period 1750-1890 and 1940-2002. However, it is not clear yet, if DOC concentrations in the most recent core part consisting of firn with densities below about 0.74 kg/L can be determined without contamination.

We acknowledge support from Sönke Szidat and the Laboratory for the Analysis of Radiocarbon with AMS (LARA).

- [1] T. M. Jenk et al., *Atmos. Chem. Phys.*, **6**, 12, 5381-5390 (2006).
 [2] M. Legrand et al., *J. Geophys. Res.*, **118**, 9, 3879-3890 (2013).

A METHOD FOR ANALYSING SECONDARY ORGANIC AEROSOLS IN ICE

A. L. Vogel (PSI), I. El-Haddad (PSI/LAC), S. Bjelić, K. Arturi (PSI/LBK), L. Fang, M. Schwikowski (PSI & Univ. Bern)

An analytical method for the sensitive detection of organic acids in glacier ice cores was developed. Solid phase extraction (SPE) was used to enrich organic acids by a factor of 200, showing quantitative recovery from the SPE column for the majority of compounds that are detected in ambient secondary organic aerosol. Analysis using liquid chromatography coupled to a high resolution Orbitrap mass spectrometer allows unambiguous determination of the elemental composition of the organic compounds.

Glaciers are valuable environmental archives that allow us to learn about the atmospheric and climatic conditions of the past. Knowledge on the state of the pre-industrial atmosphere helps us to improve global climate models, of which the uncertainty largely originates from the fact that we do not know the pre-industrial concentrations of natural aerosol particles that can act as cloud condensation nuclei (CCN) [1]. A large fraction of CCN in our atmosphere originates from secondary organic aerosol (SOA) formation that is formation of new particles in the atmosphere after oxidation and gas-to-particle conversion of volatile organic compounds (VOCs).

We developed a solid phase extraction that allows to measure oxidation products of anthropogenic and biogenic VOC emissions in glacier ice cores. A novel concept of determining the recoveries with the SPE method has been developed: we extracted ambient organic aerosols collected on filters (Jungfrauoch, Magadino, chamber α -pinene SOA), diluted the extract in water to mimic concentrations in glacier ice, and applied the developed anion exchange SPE method on the diluted extract. Knowing the quantity which corresponds to quantitative recovery for every single individual component, we are able to determine the recovery for all components that are detected by liquid chromatography coupled to electrospray ionization ultrahigh resolution mass spectrometry (LC/(-)ESI-UHRMS) in the undiluted filter extract. Although we cannot determine the exact molecular identity of each single individual component, we can attribute compound classes to individual peaks by concurrent analysis of laboratory SOA from different precursor VOCs.

As shown in Fig.1 we obtain excellent recovery ($100\% \pm 25\%$) for organic components of the elemental composition class CHO, these are compounds consisting only of carbon, hydrogen and oxygen. This class is largely dominated by biogenic secondary organic aerosol components. Organic sulfates, such as methanesulfonic acid, could not be recovered from the SPE column, since they likely bind strongly to the anion exchange material. The detected compounds were identified using a non-target screening approach

of the UHRMS data.

A first application of this method has been conducted on an ice core from Fiescherhorn glacier in the Swiss Alps, which will allow us to measure a large number of secondary organic aerosol components in glacier ice back to the 17th century, and thus depict the composition of pre-industrial aerosol over the European continent.

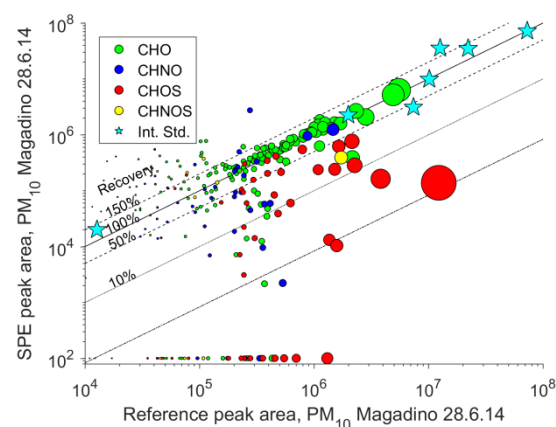


Fig. 1. Signal intensity of compounds, which are identified by a non-targeted analysis of an ambient PM10 filter sample versus the signal intensity of the same sample after dilution and enrichment using the developed solid phase extraction method.

We acknowledge the PSI Cross funding project “Reconstructions of pre-industrial organic aerosols”.

[1] K. Carslaw et al., Nature **503**, 67-71 (2013).

CO₂ IN-SITU PRODUCTION IN GREENLAND ICE

T. M. Jenk (PSI), T. Blunier (CIC)

The sources, the reason and mechanisms for the measured elevation in CO₂ concentrations in Greenland ice cores compared to coeval data from Antarctic are still not understood. This ongoing work aims at a fundamental understanding of the sources and processes involved.

Ice cores are the only environmental archive giving access to atmospheric concentrations of greenhouse gases in the past. Such records can be obtained by extracting the air from bubbles which were eventually entrapped in the ice during the firn-ice densification process [1]. However, alteration of the signal within the ice cannot per se be excluded. CO₂ measurements in ice cores from Greenland do not only result in elevated concentrations compared to the Antarctic counterpart but also display unexpected high variations of several ppm CO₂ within samples of similar gas age [2].

Both offset and variations are too large to be explained by atmospheric processes and significantly exceed analytical uncertainties. Higher temperatures and impurity content can be assumed to favour post-depositional processes in ice. CO₂ production from reactions between chemical species contained in the ice is thus likely to explain the discrepancy in CO₂ concentration and variability observed comparing measurements from Greenland and much colder and cleaner Antarctic ice.

Potential sources of CO₂ in-situ production have been proposed in the past [e.g. 2, 3] (e.g. acidification of carbonates, oxidation of aldehydes or photodecarboxylation of humic like substances) but these studies do deviate in their conclusions, leaving many questions open. Understanding would however be fundamental to assure the reliability also of Antarctic CO₂ records and, as consequence, the quality of global climate models and future climate predictions.

Our investigation of the excess CO₂ (ΔCO_2) observed in ice from Greenland is based on the combined analysis of CO₂ concentrations, $\delta^{13}\text{C}\text{-CO}_2$ and chemical impurities. This is done using samples of various ages (late-Holocene, Glacial) and depth resolution (subannual to multi-annual) from different Greenland ice cores (Eurocore, GRIP, NGRIP). Additional data from previous studies of Greenland CO₂ are used. To define the expected atmospheric CO₂ in Greenland we rely on a variety of published Antarctica firn gas and ice core CO₂ records from different sites and analysed in different laboratories. These records are combined with more recent direct observations from atmospheric stations such as Mauna Loa and we account for the interhemispheric gradient in CO₂ concentrations. The same is applied to quantify a potential offset in Greenland $\delta^{13}\text{C}\text{-CO}_2$.

In agreement with previous studies, for example [3], we can confirm an increase in ΔCO_2 with the age of the sample (Fig. 1).

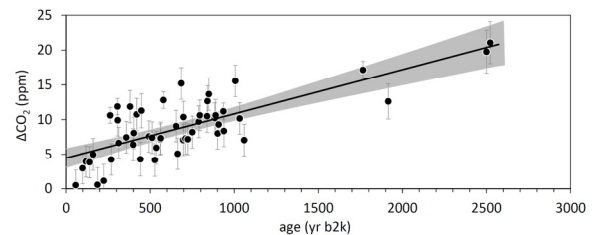


Fig. 1. Evolution of the measured offset in Greenland ice core CO₂ vs. time (in years before 2000 AD, dots). Indicated 1σ uncertainties were derived by error propagation of analytical uncertainties (both Greenland and Antarctic CO₂) and uncertainties associated with the latitudinal CO₂ gradient. The black line indicates a linear fit ($p < 0.01$, $r(50)=0.76$) with 1σ confidence band (shaded).

A solid quantification of this increase in combination with $\delta^{13}\text{C}\text{-CO}_2$ for source attribution by isotope mass-balance modeling and data of chemical impurity content allows us to get a deeper insight into the potential reactions and reaction mechanisms at place. Based on this additional knowledge we can estimate the expected CO₂ in-situ production in ice at any given temperature and impurity content. As a spoiler of the publication in progress and aiming to avoid the potential to take this short synopsis out of context, we here conclude that ice core CO₂ records from Antarctica are a highly reliable source of information.

We acknowledge funding from the Danish National Research Foundation and the European Union's Seventh Framework programme "Past4Future" (FP7/2007-2013, Grant 243908).

- [1] C. Buizert et al., *ACP*, **12**, 9 (2012).
- [2] J. Tschumi and B. Stauffer, *J. Glaciol.*, **46**, 152 (2000).
- [3] M. I. Guzmán et al., *J. Geophys. Res.*, **112**, D10123 (2007).

VOLCANOES CAST SHADOW ON MONSOON AND CLEOPATRA'S EMPIRE

M. Sigl (PSI), F. M. Ludlow (Trinity College), J. G. Manning (Yale University)

Volcanic eruptions provide tests of human and natural system sensitivity to abrupt shocks because their repeated occurrence allows the identification of systematic relationships in the presence of random variability. Here we investigated the impact of eruptive volcanism on the Nile's ability to flood.

At the heart of the ancient Egyptian society was the Nile River, the lifeblood of the Ptolemaic Kingdom. This empire arose in about 305 BC and ended around 30 BC with the death of Cleopatra. During this period, Egyptian farmers depended on the yearly flooding of the Nile in July through September to irrigate their grain fields – inventing systems of channels and dams to store the river's overflow. When the Nile flood was good, the Nile valley was one of the most agriculturally-productive places in the Ancient World, but the river was famously prone to a high level of variation.

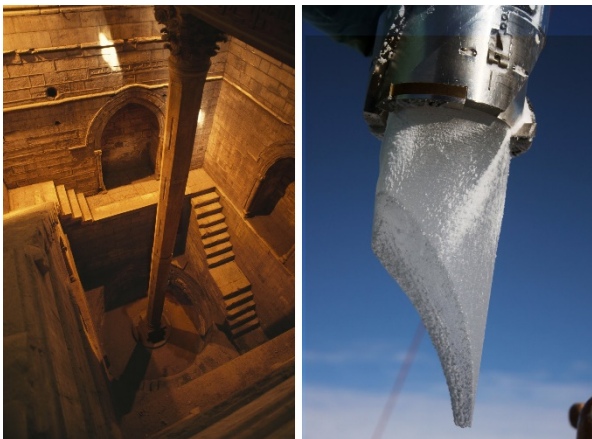


Fig. 1. (Left) the Rawdah Nilometer in Cairo, providing annual measurements of the Nile river summer flood height between 622-1902 AD; (right) an ice core taken from NE Greenland was used to infer volcanic eruption dates. Credit: Left, Richard Nowitz/National Geographic, via Getty Images; right, M. Sigl

Combining volcano-climate numerical modeling, ice-core catalogued eruption timings, ancient Egyptian documentation of socio-economic behaviour, and recordings from the Islamic Nilometer (an ancient history of Nile water levels, Fig. 1), we demonstrate that the lack of critically important summer flooding over the past millennia, including in Ptolemaic Egypt, correlates with volcanic eruptions [1] and is causally linked via the radiative and dynamical impacts of explosive volcanism on the African monsoon [2].

Our previous understanding of the role of volcanism on climate and ancient societies was limited by the lack of a complete record of global volcanism with well-constrained evidence of timing and magnitudes of stratospheric sulphate aerosol injections. Ice-cores

obtained from polar ice sheets are arguably the best archive for reconstructing the history of global volcanism over past millennia, but undiagnosed chronological errors had for a long time hampered a systematic determination of a volcanic impact on climate and society before the second millennium AD. Recent revisions made to polar ice-core chronologies [3] have significantly reduced dating uncertainties and allowed us now for the first time to systematically track the impact of volcanic eruptions on the climate system and human societies further back in time, including ancient Egypt.

We further examined the response of Ptolemaic Egypt, one of the best-documented ancient superpowers, to volcanically induced Nile suppression (Fig. 2). Eruptions are frequently associated with revolt onset against elite rule. Eruptions are also followed by socioeconomic stress with increased land sales, and the issuance of priestly decrees to reinforce elite authority. Ptolemaic vulnerability to volcanic eruptions offers a caution for all monsoon-dependent agricultural regions, presently including 70% of the world population.

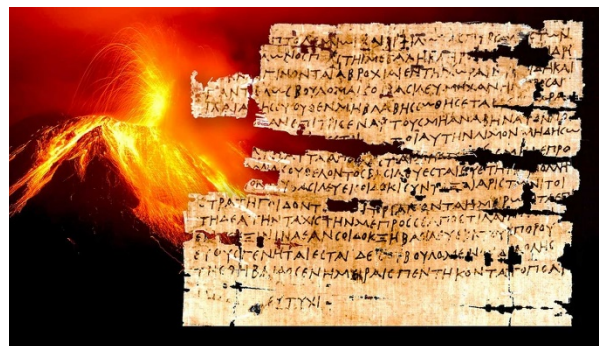


Fig. 2. With the ice-core timeline it was possible to link major volcanic eruptions (background) to the suppression of flooding on the Nile River (foreground), for details see [1]. The text above is from the Edfu papyrus. Graphic: Joseph Manning; Papyrus: © Department of Papyrology, Institute of Archaeology, University of Warsaw

This work is as a result of the authors' participation in the Past Global Changes (PAGES) Volcanic Impacts on Climate and Society (VICS) working group.

- [1] J. G. Manning et al., *Nat. Commun.*, **8**, 900 (2017).
- [2] C. E. Iles & G. C. Hegerl, *Nat. Geosci.* **8**, 836-837 (2015).
- [3] M. Sigl et al., *Nature*, **523**, 536-549 (2015).

RECONSTRUCTED ACCUMULATION RATES AT QUELCCAYA ICE CAP

T. M. Jenk, S. Brüttsch (PSI), D. Hardy (UMass), M. Vuille (Univ. Albany), M. Schwikowski (PSI & Univ. Bern)

By combining data from yearly snowpit sampling and a 21 m firn core taken in 2014, annual net accumulation rates for the summit of the Quelccaya Ice Cap have been reconstructed for 2000-2015. They allow for a first direct comparison with high altitude automated weather station measurements.

The Quelccaya Ice Cap is situated in a climatically sensitive region and its size decreased by >30% over the last 35 years. With ice cores being drilled to bedrock in 1983 and 2003, has well been studied for more than 40 years. Since 2003, an automated weather station (AWS) is operated at the summit and in 2014, a 21 m long firn core was drilled closeby for overlap of data [1 and therein, 2].

Here we present combined results from the 2014 core (C) and yearly sampled snow pits (P) expanding the 2003 ice core record to the year of the strong El Nino in 2016, overlapping with the full time period of AWS measurements.

Accurate matching on a common depth scale of snow pit and ice core data was achieved by transferring measured sampling depth into meter water equivalent (m w.e.) using the Black Carbon (BC) records and a combined P and C density profile (Fig. 1). Shown in Fig. 2a, major ions generally show strong decrease in amplitude from one to the next sampling period (e.g. acetate, NH_4^+ , SO_4^{2-}) with various degree of smoothing (especially severe for $\delta^{18}\text{O}$). While most ionic species get increasingly washed out with depth, the signal of the highly soluble acetate is lost almost entirely within one annual cycle but an increase in concentrations was observed at a depth of ~ 7 m w.e.. This depth coincides with the depth where complete smoothing of the $\delta^{18}\text{O}$ signal is reached (Fig. 2b). This is strong indicator for mass redistribution over several m of firn. Redistribution over shorter distances, sometimes within one annual layer only, is indicated by the formation of new ice lenses observed when resampling in subsequent years. In such layers, concentrations are often increased (e.g. SO_4^{2-} at 4 to 5 m w.e., Fig. 2a, b). No effect of post-depositional processes was observed for BC, allowing counting of annual layers (ALC). From the known dates of sampling campaigns the peak maxima could be related to August (Fig. 2b).

ALC reveals a continuous record (2000-2016) allowing calculation of the net annual accumulation (b_{PC} , Aug. to Aug.). Comparing b_{PC} with the AWS derived net accumulation rates (calculated from changes relative to the 2003 surface) shows good agreement in annual variations but an offset in absolute values (b_{net} , defined as wet season accumulation, b_{wet} , minus the dry season accumulation loss b_{dry}), see Fig. 2c. In agreement with [1], we attribute this mismatch to uncertainties when surface height changes need to be transferred to m w.e. due to the lack of precise

knowledge about the time resolved firn densification process. The close relation between the observed offset ($\Delta b_{\text{PC}} - b_{\text{net}}$) with b_{dry} , indicates this to particularly effect dry season measurements, when warmer temperatures and thus assumingly enhanced densification persists. Our data indicates overestimation of b_{dry} , which at least partly should be attributed to densification instead of loss. Whether the better agreement with the early AWS record is related to the recent increase in site temperature (enhanced densification) or to the fact that the base of the AWS was placed in not yet fully densified firn when mounted in 2003, causing the early measurements to be (partly) adjusted by simultaneous, densification-induced base lowering is subject of ongoing work.

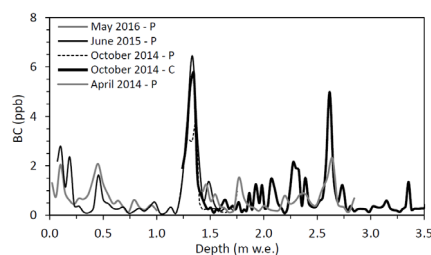


Fig. 1. Overlap and matching of BC records from snow pits (P) and ice core (C) on a common depth scale.

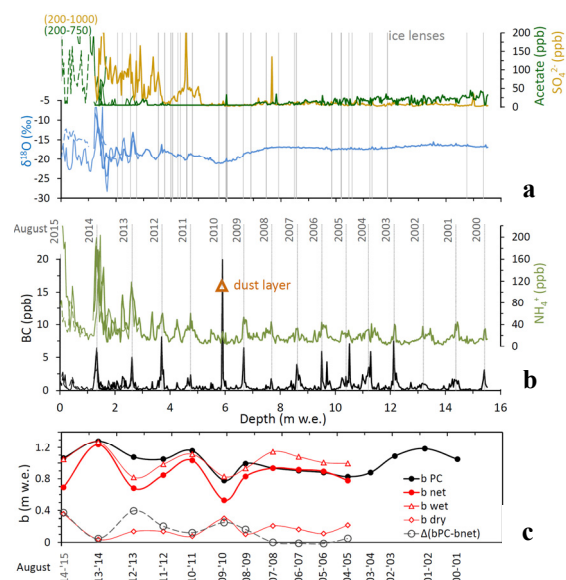


Fig. 2. a, b) Combined snow pit (thin lines; dashed for the May 2016 pit) and ice core record of various parameters, stratigraphy and ALC (peak in Aug.). **c)** Reconstructed accumulation (b_{PC}) and AWS b_{net} , b_{wet} and dry season loss (b_{dry}) with offset $\Delta(b_{\text{PC}} - b_{\text{net}})$.

- [1] C. D. Chadwell et al., TCD, in review (2016).
 [2] T. M. Jenk et al., Ann. Rep. Lab. of Radio- & Environm. Chem., p. 22 (2014).

ICE CORE DRILLING ON TEMPERATE RHONEGLETSCHER

M. Schwikowski (PSI & Univ. Bern), T. M. Jenk (PSI), D. Stampfli (icedrill.ch), S. Hellmann, A. Bauder (ETHZ)

An ice core was collected in August 2017 at the temperate Rhonegletscher for ice fabric analyses. The resulting crystal size and orientation data will serve to investigate anisotropy patterns in radar and seismic wave velocities in ice.

Glaciers respond sensitively to climate fluctuations and their severe retreat is one of the clearest natural indicators of ongoing climate change. To assess their state and dynamical behavior, knowledge of the physical properties of the ice mass and its bed characteristics is required. Since both of these features are generally not directly accessible, geophysical methods like ground-penetrating-radar (GPR) and seismic techniques are applied. However, the anisotropy of the electrical and elastic ice properties, further complicated by an interaction of cracks, crevasses, ice fabric and potentially by layered impurities, result in anisotropy patterns of the GPR and seismic velocities.

In this project for the first time a comprehensive 3D characterization of an ice mass using GPR and seismic techniques is conducted at Rhonegletscher, Swiss Alps. To calibrate the geophysical results we drilled an ice core in the period from 8 to 13 August 2017 using our new thermal ice drilling system [1] (Fig. 1). This was required for the conditions of Rhonegletscher, which is a temperate glacier with ice temperatures at the pressure melting point (i.e. near 0°C) from the surface down to bedrock and is strongly affected by melting. Thus, a significant amount of liquid meltwater is present, percolating within the solid ice matrix. To record the orientation of the ice cores, a parameter normally not required, the drill was modified by adding a magnetic field logger with the corresponding housing. 46.12 m core were drilled in a first borehole, when drilling had to be stopped. Sudden drainage of the water-filled borehole had caused overheating of the coil heater, breaking its aluminium crown. The aluminium parts blocked the borehole prevented further penetration. In a second borehole predrilled down to 52 m with a hot-water drill, ice core drilling was continued to a depth of 80.55 m, where a cm-size stone was encountered and drilling was stopped (Fig. 2). Overall 75 m ice cores were recovered in 69 h, equivalent to an ice core production rate of 2.23 m/h, which is slightly higher than the 1.8 m/h achieved on Silvrettagletscher [1].

Almost all cores from the surface to 80.55 m consisted of alternating layers of bubbly ice and clear ice with large cm-size single crystals (Fig. 3). Only close to 80 m depth clear ice dominated. The ice cores were transported frozen to PSI and cut in samples for ice fabric analysis, which is ongoing work at the Alfred Wegener Institute for Polar and Marine Research in Bremerhaven.



Fig. 1. Ice core drilling tent in the ablation zone of Rhonegletscher.

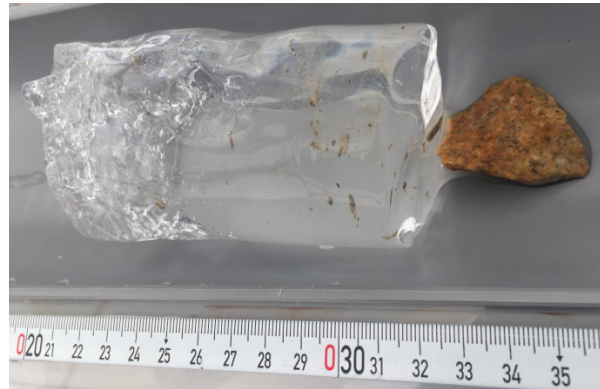


Fig. 2. Bottom most ice core piece with the stone attached to it.



Fig. 3. Exemplary image for fabric analysis of a 10 cm long piece of this ice core (turned by 90°).

We acknowledge funding from the Swiss National Science Foundation (Grant 200021_169329).

- [1] Schwikowski et al., *Ann. Glac.*, **55**, 131-136 (2014).

SEARCH FOR A GLACIER IN THE CENTRAL ANDES SUITABLE AS ICE ARCHIVE

M. Schwikowski (PSI & Univ. Bern), S. Brütsch, T. M. Jenk (PSI), A. Rivera (CECS)

The Central Andes of Chile is a heavily populated region with high atmospheric industrial urban pollution and heavy mining activities. The regional glaciers have experienced a strong retreat and darkening in recent decades. How much the emissions from mining and urban/industrial activities contribute to glacier darkening is an open question. We analysed a shallow ice core from Cerro Negro glacier to investigate its suitability for reconstructing environmental conditions.

The 7.43 m long ice core collected on Cerro Negro (33°08'37.5" S, 70°13'38.5" W, 4604 m asl.) in Chile on 30 April 2017, was chemically analyzed at PSI. The core was processed in 5 cm resolution, resulting in overall 142 samples. Visual stratigraphy, ice density, stable isotope ratios ($\delta^{18}\text{O}$, $\delta^2\text{H}$, dexcess), concentrations Na^+ , NH_4^+ , K^+ , Mg^{2+} , Ca^{2+} , F^- , CH_3COO^- , HCOO^- , CH_3SO_3^- ; Cl^- , NO_3^- , SO_4^{2-} , $\text{C}_2\text{O}_4^{2-}$, and black carbon (BC).

Visual stratigraphy showed the presence of superimposed ice formed by refreezing of surface meltwater already for the topmost core. The ice contains few air bubbles, consistent with a high density of 0.92 g/cm^3 . Both findings confirm the strong influence of melt processes (Fig. 1).

The concentration records of chemical trace species (major ions and BC) are characterized by a major peak in the upmost 40 cm water equivalent (w.e., depth scale adjusted to water density), coinciding with a dark layer (Fig. 2). Only K^+ and BC show another even larger peak at ca. 17 cm w.e. In the remaining deeper part of the core the concentrations are much lower, with less variability. We interpret this finding as enrichment of impurities at the surface by melting, meltwater percolation, meltwater run-off and to a lesser degree sublimation, resulting in removal of the snow matrix. This enrichment might have happened over a time period of several years. As a consequence the age of the surface is unknown and cannot be determined with standard methods. Below 40 cm w.e. depth the records of chemical impurities are strongly affected by melt processes, resulting in a nearly complete removal of the signal of the water soluble major ions, but also of particulate BC. The average concentrations are significantly lower than in the surface layer, but also compared to other ice cores from the Central Andes, i.e. Cerro Plomo 11 km further south and Mercedario on the Argentinian side of the Andes, 130 km to the north [1].

The record of the stable isotope ratio $\delta^{18}\text{O}$ also shows little variation, but in this case the average is similar to

the one of Cerro Plomo [1].

Overall the results suggest that the records are strongly biased by melt processes and can therefore not be used to deduce information about past input of air pollution. Assuming that the in total 11 small peaks in BC represent annual enrichment layers, an average net accumulation of 0.7 m w.e. would result. However, with this approach years with negative local mass balance cannot be identified and are therefore not taken into account.



Fig. 1. Photo of the topmost core from Cerro Negro glacier showing transparent ice with few air bubbles and a ca. 8 cm thick dark layer at ca. 40-48 cm depth.

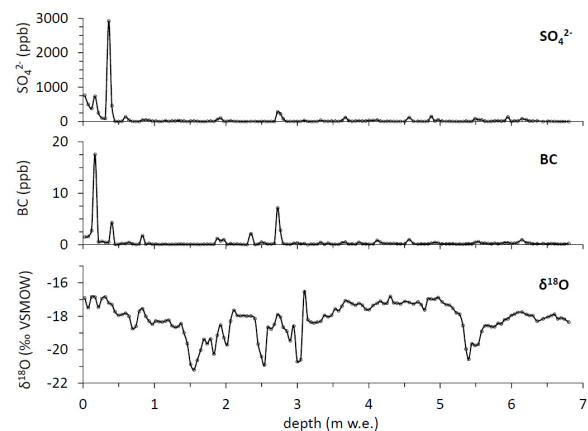


Fig. 2. Cerro Negro ice core records of $\delta^{18}\text{O}$ and the concentrations of BC and SO_4^{2-} versus depth in m w.e.

- [1] D. Bolius et al., *Ann. Glac.*, **43**, 14 (2006).

LIST OF PUBLICATIONS

SURFACE CHEMISTRY

P. A. Alpert, R. Ciuraru, S. Rossignol, M. Passananti, L. Tinel, S. Perrier, Y. Dupart, S. S. Steimer, M. Ammann, D. J. Donaldson and C. George

Fatty acid surfactant photochemistry results in new particle formation

Scientific Reports **7**, 12693, doi: 10.1038/s41598-017-12601-2

L. Artiglia, J. Edebeli, F. Orlando, S. Chen, M.-T. Lee, P. Corral Arroyo, A. Gilgen, T. Bartels-Rausch, A. Kleibert, M. Vazdar, M. Andres Carignano, J. S. Francisco, P. B. Shepson, I. Gladich and M. Ammann

A surface-stabilized ozonide triggers bromide oxidation at the aqueous solution-vapour interface

Nature Communications **8**, 700, doi: 10.1038/s41467-017-00823-x

L. Artiglia, F. Orlando, K. Roy, R. Kopelent, O. Safonova, M. Nachtegaal, T. Huthwelker and J. A. van Bokhoven

Introducing time resolution to detect Ce^{3+} catalytically active sites at the Pt/CeO₂ interface through ambient pressure X-ray photoelectron spectroscopy

Journal of Physical Chemistry Letters **8** (1), 102-108, doi: 10.1021/acs.jpcclett.6b02314

F. Barsotti, T. Bartels-Rausch, E. De Laurentiis, M. Ammann, M. Brigante, G. Mailhot, V. Maurino, C. Minero and D. Vione

Photochemical formation of nitrite and nitrous acid (HONO) upon irradiation of nitrophenols in aqueous solution and in viscous secondary organic aerosol proxy

Environmental Science and Technology **51**, 7486-7495, doi: 10.1021/acs.est.7b01397

T. Bartels-Rausch, F. Orlando, X. Kong, L. Artiglia and M. Ammann

Experimental evidence for the formation of solvation shells by soluble species at a nonuniform air-ice interface

ACS Earth and Space Chemistry **1**, 572-579, doi: 10.1021/acsearthspacechem.7b00077

T. Berkemeier, M. Ammann, U. K. Krieger, T. Peter, P. Spichtinger, U. Pöschl, M. Shiraiwa and A. J. Huisman

Technical note: Monte Carlo genetic algorithm (MCGA) for model analysis of multiphase chemical kinetics to determine transport and reaction rate coefficients using multiple experimental data sets

Atmospheric Chemistry and Physics **17**, 8021-8029, doi: 10.5194/acp-17-8021-2017

M. Bruggemann, N. Hayeck, C. Bonnineau, S. Pesce, P. A. Alpert, S. Perrier, C. Zuth, T. Hoffmann, J. Chen and C. George

Interfacial photochemistry of biogenic surfactants: a major source of abiotic volatile organic compounds

Faraday Discussions **200**, 59-74 (2017), doi: 10.1039/C7FD00022G

J. B. Burkholder, J. P. D. Abbatt, I. Barnes, J. M. Roberts, M. L. Melamed, M. Ammann, A. K. Bertram, C. D. Cappa, A. G. Carlton, L. J. Carpenter, J. N. Crowley, Y. Dubowski, C. George, D. E. Heard, H. Herrmann, F. N. Keutsch, J. H. Kroll, V. F. McNeill, N. L. Ng, S. A. Nizkorodov, J. J. Orlando, C. J. Percival, B. Picquet-Varrault, Y. Rudich, P. W. Seakins, J. D. Surratt, H. Tanimoto, J. A. Thornton, Z. Tong, G.S. Tyndall, A. Wahner, C. J. Weschler, K. R. Wilson and P. J. Ziemann

The essential role for laboratory studies in atmospheric chemistry

Environmental Science and Technology **51**, 2519-2528, doi: 10.1021/acs.est.6b04947

S. China, P. A. Alpert, B. Zhang, S. Schum, K. Dzepina, K. Wright, R. C. Owen, P. Fialho, L. R. Mazzoleni, C. Mazzoleni and D. A. Knopf

Ice cloud formation potential by free tropospheric particles from long-range transport over the Northern Atlantic Ocean

Journal of Geophysical Research: Atmospheres **122**, 3065-3079, doi: 10.1002/2016JD025817

I. Coluzza, J. Creamean, M. Rossi, H. Wex, P. A. Alpert, V. Bianco, Y. Boose, C. Dellago, L. Felgitsch, J. Fröhlich-Nowoisky, H. Herrmann, S. Jungblut, Z. Kanji, G. Menzl, B. Moffett, C. Moritz, A. Mutzel, U. Pöschl, M. Schauperl, J. Scheel, E. Stopelli, F. Stratmann, H. Grothe and D. Schmale

Perspectives on the future of ice nucleation research: research needs and unanswered questions identified from two international workshops

Atmosphere **8**, 138, doi:10.3390/atmos8080138

G. Gržinić, T. Bartels-Rausch, A. Türler and M. Ammann

Efficient bulk mass accommodation and dissociation of N₂O₅ in neutral aqueous aerosol

Atmospheric Chemistry and Physics **17**, 6493-6502, doi: 10.5194/acp-17-6493-2017

X. Kong, A. Waldner, F. Orlando, L. Artiglia, T. Huthwelker, M. Ammann and T. Bartels-Rausch
Coexistence of physisorbed and solvated HCl at warm ice surfaces
Journal of Physical Chemistry Letters **8** (19), 4757-4762, doi: 10.1021/acs.jpcllett.7b01573

H. Meusel, Y. Elshorbany, U. Kuhn, T. Bartels-Rausch, K. Reinmuth-Selzle, C. J. Kampf, G. Li, X. Wang, J. Lelieveld, U. Pöschl, T. Hoffmann, H. Su, M. Ammann and Y. Cheng
Light-induced protein nitration and degradation with HONO emission
Atmospheric Chemistry and Physics **17**, 11819-11833 (2017), doi: 10.5194/acp-17-11819-2017

ANALYTICAL CHEMISTRY

P. Bohleber, L. Sold, D. R. Hardy, M. Schwikowski, P. Klenk, A. Fischer, P. Sirguy, N. J. Cullen, M. Potocki, H. Hoffmann and P. Mayewski
Ground-penetrating radar reveals ice thickness and undisturbed englacial layers at Kilimanjaro's Northern Ice Field
The Cryosphere **11**, 469-482, doi: 10.5194/tc-11-469-2017

A. Eichler, G. Gramlich, T. Kellerhals, L. Tobler, T. Rehren and M. Schwikowski
Ice-core evidence of earliest extensive copper metallurgy in the Andes 2700 years ago
Scientific Reports **7**, 41855, doi: 10.1038/srep41855

M. Engardt, D. Simpson, M. Schwikowski and L. Granat
Deposition of sulphur and nitrogen in Europe 1900–2050. Model calculations and comparison to historical observations
Tellus B **69**, 1328945, doi: 10.1080/16000889.2017.1328945

S. Eyrikh, A. Eichler, L. Tobler, N. Malygina, T. Papina and M. Schwikowski
A 320 year ice-core record of atmospheric Hg pollution in the Altai, Central Asia
Environmental Science and Technology **51** (20) 11597-11606, doi: 10.1021/acs.est.7b03140

P. D. Henne, M. Bigalke, U. Büntgen, D. Colombaroli, M. Conedera, U. Feller, D. Frank, J. Fuhrer, M. Grosjean, O. Heiri, J. Luterbacher, A. Mestrot, A. Rigling, O. Rössler, C. Rohr, T. Rutishauser, M. Schwikowski, A. Stampfli, S. Szidat, J.-P. Theurillat, R. Weingartner, W. Wilcke and W. Tinner
An empirical perspective for understanding climate change impacts in Switzerland
Regional Environmental Change **18** (1), 205-221, doi: 10.1007/s10113-017-1182-9

R. S. Ødegård, A. Nesje, K. Isaksen, L. M. Andreassen, T. Eiken, M. Schwikowski and C. Uglietti
Climate change threatens archaeologically significant ice patches: insights into their age, internal structure, mass balance and climate sensitivity
The Cryosphere **11**, 17-32, doi: 10.5194/tc-11-17-2017

J. Schmale, M. Flanner, S. Kang, M. Sprenger, Q. Zhang, J. Guo, Y. Li, M. Schwikowski and D. Farinotti
Modulation of snow reflectance and snowmelt from Central Asian glaciers by anthropogenic black carbon
Scientific Reports **7**, 40501, doi: 10.1038/srep40501

AFFILIATION INDEX

ANU	The Australian National University, Research School of Earth Sciences, Acton ACT 2601, Australia
BAS	British Antarctic Survey, High Cross, Madingley Road, Cambridge CB3 0ET, UK
CECs	Centro de Estudios Científicos, Arturo Prat 514, Valdivia, Chile
CIC	Niels Bohr Institute, Center for Ice and Climate, University of Copenhagen, Juliane Maries Vej 30, 2100 Copenhagen, Denmark
EMPA	Materials Science and Technology, Überlandstrasse 129, 8600 Dübendorf, Switzerland
ETHZ	Eidgenössische Technische Hochschule Zürich, 8092 Zürich, Switzerland
HBKU	Hamad Bin Khalifa University, Education City, Doha, Qatar
GIT	Georgia Institute of Technology, 311 Ferst Drive, Atlanta, GA 30332-0100, USA
icedrill.ch	icedrill.ch AG, Schuetzengasse 172, 2502 Biel, Switzerland
IRCELYON	Institut de Recherches sur la Catalyse et l'Environnement de Lyon, 2 avenue Albert Einstein, 69626 Villeurbanne cedex, France
LAC	Laboratory of Atmospheric Chemistry, Paul Scherrer Institut, 5232 Villigen, Switzerland
LATMOS	Laboratoire Atmosphères, Milieux, Observations Spatiales, 11 Boulevard D'Alembert, 78280 Guyancourt, France
LBK	Bioenergy and Catalysis Laboratory, Paul Scherrer Institut, 5232 Villigen, Switzerland
LMN	Laboratory for Micro and Nanotechnology, Paul Scherrer Institut, 5232 Villigen, Switzerland
LSC	Laboratory for Condensed Matter, Paul Scherrer Institut, 5232 Villigen, Switzerland
LSF	Laboratory for Femtochemistry, Paul Scherrer Institut, 5232 Villigen, Switzerland
LSK	Laboratory for Catalysis and Sustainable Chemistry, Paul Scherrer Institut, 5232 Villigen, Switzerland
MPIC	Max-Planck-Institut für Chemie (Otto-Hahn-Institut), Joh.-Joachim-Becher-Weg 27, 55128 Mainz, Germany
PSI	Paul Scherrer Institut, 5232 Villigen, Switzerland
RBI	Ruder Bošković Institute, Bijenička cesta 54, 10000 Zagreb, Croatia
Trinity College	Trinity College Dublin, The University of Dublin, College Green, Dublin 2, Ireland
Univ. Aberystwyth	Aberystwyth University, Penglais, Aberystwyth, Ceredigion, SY23 3FL, UK
Univ. Albany	Department of Atmospheric and Environmental Sciences, University at Albany, State University of New York, Albany, NY 12222, USA
Univ. Bern	Departement für Chemie und Biochemie, Universität Bern, Freiestrasse 3, 3012 Bern, Switzerland
Univ. Gothenburg	Department of Chemistry and Molecular Biology, University of Gothenburg, Vasaparken, 405 30 Gothenburg, Sweden
Univ. Pavia	Department of Electrical, Biomedical and Computer Engineering, University of Pavia, Via Ferrata, 5, 27100 Pavia, Italy
Univ. Venice	Department of Environmental Sciences, Ca'Foscari University of Venice, Dorsoduro 213, 30123 Venice, Italy
UCI	Department of Chemistry, University of California, 1102 Natural Sciences 2, Irvine, CA 92697-2025, USA
UMass	Department of Geosciences, University of Massachusetts, 134 Morrill Science Center II, Amherst, MA 01003, USA
UNL	Department of Chemistry, University of Nebraska-Lincoln, 433 Hamilton Hall, Lincoln, NE 68588-0304, USA
WSL-SLF	Swiss Federal Institute for Forest, Snow and Landscape Research WSL, 8903 Birmensdorf, Switzerland
XMU	Xiamen University, No. 422, Siming South Road, Xiamen, Fujian, China 361005
Yale University	Department of History, Yale University, 320 York Street, New Haven, CT 06520-8324, USA

